A Two-Scale Approximation for Efficient Representation of Nonlinear Energy Transfers in a Wind Wave Spectrum. Part II: Application to Observed Wave Spectra

WILLIAM PERRIE

Bedford Institute of Oceanography, Fisheries and Oceans Canada, Dartmouth, Nova Scotia, Canada

DONALD T. RESIO

Coastal and Hydraulics Laboratory, Engineer Research and Development Center, Vicksburg, Mississippi

(Manuscript received 5 November 2007, in final form 11 February 2009)

ABSTRACT

In Part I of this series, a new method for estimating nonlinear transfer rates in wind waves, based on a two-scale approximation (TSA) to the full Boltzmann integral (FBI) for quadruplet wave–wave interactions, was presented, and this new method was tested for idealized spectral data. Here, the focus is on comparisons of the TSA and the discrete interaction approximation (DIA) with the FBI for observed wave spectra from field measurements. Observed wave spectra are taken from a wave gauge array in Currituck Sound and a directional waverider off the coast near the Field Research Facility at Duck, North Carolina. Results show that the TSA compares much more favorably to the FBI than does the DIA, even for cases in which the parametric component of the formulation does not capture the spectral energy distribution very well. These results remain valid for the TSA estimates when the FBI results are significantly affected by the directional distribution of energy. It is also shown that although nonlinear transfers are substantially weaker in swell portions of the spectrum these interactions contribute significantly to the spectral evolution and net energy balance in long-distance swell propagation.

1. Introduction

As discussed in Resio and Perrie (2008, hereafter Part I), nonlinear wave–wave interactions involving quadruplets constitute the basis for modern wave modeling. In most modern operational wave models such as the Wave Analysis Model (WAM), quadruplet wave–wave interactions are simulated by the discrete interaction approximation, commonly referred to as the DIA, as formulated by Hasselmann et al. (1988). Part I introduced a new approximation, the two-scale approximation (TSA), based on the separation of a spectrum into a broad-scale component and a local-scale (perturbation) component. The TSA uses a parametric representation of the broad-scale spectral structure while preserving the degrees of freedom essential to a detailed-balance source term formulation, by including the second-order scale in the approximation. Part I presented tests using idealized wave spectra, including Joint North Sea Wave Project (JONSWAP) spectra (Hasselmann et al. 1973) with selected peakednesses, finite-depth tests, and perturbation cases. For the idealized cases shown in Part I, the results suggest that the TSA can provide significantly increased accuracy in representations of nonlinear energy transfers relative to the DIA. Here, to investigate the ability of the TSA to replicate nonlinear energy transfers in more general situations, comparisons will be made with the full Boltzmann integral (FBI) using measured field spectra.

In this paper, we present comparisons between the three formulations—TSA, DIA, and FBI—using observed deep-water wave spectra from Currituck Sound (North Carolina), and in open-ocean conditions from a directional waverider located off the U.S. Army Field Research Facility at Duck (North Carolina) during Hurricane Wilma in 2005. The observed data from Currituck Sound were collected from a wave-staff array as described by Long and Resio (2007). The data are two-dimensional (2D) spectra in deep-water fetch-limited

Corresponding author address: William Perrie, Bedford Institute of Oceanography, 1 Challenger Dr., Dartmouth, NS B2Y 4A2, Canada.
E-mail: perriew@dfo-mpo.gc.ca

DOI: 10.1175/2009JPO3947.1

conditions, in onshore and offshore wind conditions, and in slanting-fetch conditions. Each Currituck Sound case represents a composite spectrum, consisting of data that were carefully analyzed from multiple measurements. Observations from open-ocean conditions were collected by a waverider during Hurricane Wilma and consist of individual ocean directional wave spectra, as the storm moved northeastward from Florida, passing near Cape Hatteras.

Section 2 presents an overview description of the observed wave data from Currituck Sound and Hurricane Wilma. Section 3 compares results from the three nonlinear spectra (S_{nl}) formulations using the wave spectra from Currituck Sound. Section 4 compares results from Hurricane Wilma wave data. Section 5 discusses a special case of bimodal spectra with mixed sea and swell data, and section 6 discusses the implications of our results on conventional scaling arguments for nonlinear interactions and the spectral evolution of swell from large storms. Section 7 summarizes our results and provides conclusions.

2. Observed wave spectra

a. Currituck Sound wave observations

The wave data collected in Currituck Sound are described and analyzed in detail by Long and Resio (2007). These are hourly observations of directional wave spectra and local winds as obtained at a fixed location on the east side of Currituck Sound (denoted "sled" in Fig. 1) near the Field Research Facility (FRF) during the period from 24 October 2001 to 19 April 2002. Wave data were recorded by a directional wave gauge consisting of a spatial array of nine capacitance-type wave rods, configured so that it is compatible with energetic wind wave frequencies of the Currituck Sound. The sound is an elongated body of water situated between the North Carolina Outer Banks and the mainland. Fetches are as short as 0.5 km to the east and 5.5 km to the west, although there are longer fetches to the northwest and southwest. Water depths vary from 1.8 to 2.4 m over a relatively large area in the vicinity of the observation location. Wave data were analyzed using the reliable iterative maximum likelihood estimator (IMLE) of Pawka (1983) and Long (1995).

As described by Long and Resio (2007), data collection consisted of synchronous, 12 288-point sampling of wave array outputs at 0.2048-s intervals (about 4.88 Hz). This resulted in records of about 41-min duration starting at the top of each hour. As presented by Long and Resio (2007), the 2.44-Hz Nyquist frequency is compatible with the minimum gauge spacing of the directional array. Fourier analysis with segment and band

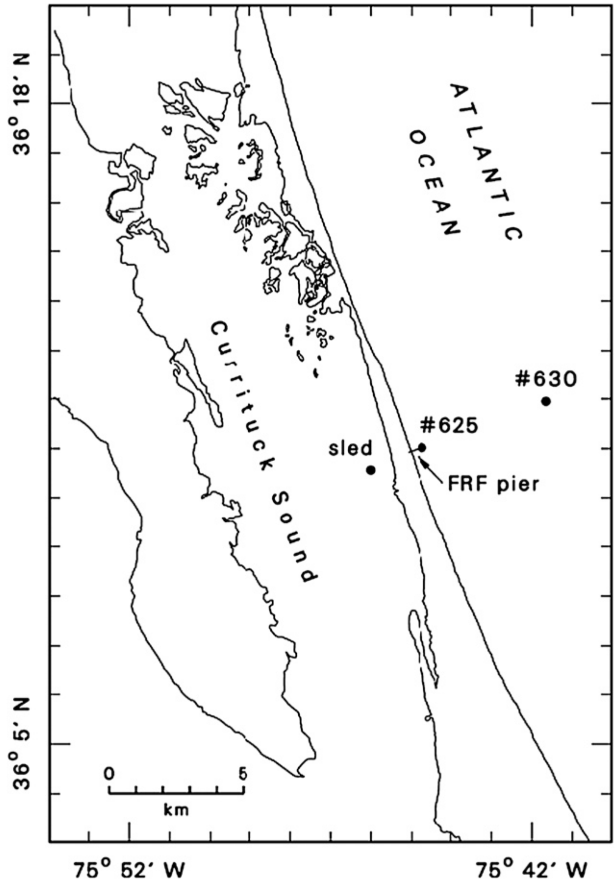

FIG. 1. Location of the observation wave-staff array (filled circle labeled "sled") in Currituck Sound. A broad channel of about 2.5-m depth runs along the long axis of the sound in the vicinity of the sled. The opening to the south, representing an arc of about 20° from the sled location, leads to Albemarle Sound, which is larger and deeper.

averaging yielded auto- and cross-spectral estimates having 120 degrees of freedom in bands of about 0.024-Hz width. Long and Resio (2007) averaged autospectral estimates from the nine wave rods to get an estimate of total variance density $E(f)$ at each frequency. The IMLE provided estimates of the directional distribution function $D(f, \theta)$, where the frequency-direction spectrum is

$$E(f,\theta) = E(f)D(f,\theta), \tag{1}$$

where θ is relative to sled coordinates and, in the rectangular (rather than polar) coordinate system used here, the distribution function is normalized and, for any given frequency f, satisfies

$$\int_0^{2\pi} D(f,\theta)\,d\theta = 1. \tag{2}$$

Resulting Currituck Sound wave spectra vary with wave age and wind direction, particularly for wind angles oblique to the shore. One-dimensional spectra were grouped into five classes of inverse wave age U_{10}/C_p ranging from 1.5 to 4.0 with bin widths of 0.5 and 18 classes of wind direction of 20° bin widths, which collectively span a full circle, as shown in Fig. 2, where U_{10} is the 10-m reference wind speed and C_p is the phase velocity at the spectral peak. Because of narrow- and slanting-fetch geometries within the sound, some of the spectra tend to be directionally sheared and misaligned with respect to local winds near their spectral peaks. Wave data include spectra for which effects of the side boundaries of the sound are negligible, as well as data for which side boundary effects are very evident. In the former case, waves resulting from an arc of angles about 60° wide centered on westerly winds exhibit minimal side boundary effects.

Directional narrowness of spectral peaks, increasing directional spreads at higher wavenumbers, and a persistent tendency for high-wavenumber distributions to be directionally bimodal are evident. Skewing of directional peaks away from oblique wind directions and toward long-fetch directions is apparent, especially in wind-direction classes near class m, for which winds and peak wave directions are aligned with the southern opening of the sound. Classes l and k, at 20° and 40° on the negative side of class m, respectively, have peak directions also about 20° and 40°, respectively, positive to the wind, and are evidently strongly influenced by the long fetch of class m. A more complex pattern occurs in classes b, c, d, and e, with primary and secondary peaks offset from the wind, possibly because of more-complicated fetch boundaries to the north and northwest. Directional shear near spectral peaks is less pronounced in classes h, i, and j, which appear to be more characteristic of cases with broad-fetch, shore-normal winds.

When side boundary effects are negligible, the wave spectra have almost constant relative peakedness of $\gamma_r \approx 2.5$. Here *relative peakedness* γ_r is defined as $\gamma_r = k_P F(k_P)/\beta$, following Long and Resio (2007); $F(k_P)$ is the energy density; k_p is the peak wavenumber; and β is a wave steepness parameter type defined as

$$\beta = 0.5\alpha_4 u g^{-1/2}, \tag{3}$$

where u is a scale velocity, g is the gravitational acceleration, and α_4 is a dimensionless universal coefficient suggested by parameterizations of the deep-water spectral equilibrium range having an f^{-4} form (Resio and Perrie 1989; Long and Resio 2007, and many others cited therein), where

$$E(f) \sim \alpha_4 u g (2\pi)^{-3} f^{-4}. \tag{4}$$

Details on the precise computation of β can be found in appendix A of Resio et al. (2004). For wave spectra influenced by the side boundaries, the directional shear in the spectral peak region is similar to that observed by Donelan et al. (1985).

The Currituck Sound wave dataset consists of composite spectra grouped into five classes of inverse wave age ranging from 1.5 to 4.0 with bin widths of 0.5 and 18 classes of wind direction using 20° bin widths, which collectively span a full circle (18 classes of 20° width, with 2 of the 18 classes having too few observations to average). The highest relative frequency bins are $f/f_p = 3.5$. Figures 2a–p qualitatively illustrate the 16 mean directional distributions, referenced to the basin boundaries in Fig. 1 for each of the wind-direction classes, relative to mean wind direction. Resulting spectra suggest narrow directional distributions near spectral peak wavenumbers and broad distributions at higher wavenumbers. The broad directional distributions at high wavenumbers in Figs. 2c–n have two modal peaks with arc $\Delta\theta$ separating of about 100° at higher wavenumbers, similar to results of Young et al. (1995), Ewans (1998), and Wang and Hwang (2001).

Figures 2c–n have directional distributions that are approximately symmetric about the mean wind direction for $f/f_p > 2.1$, with the mean wave direction tending to align with the wind direction. For the lower part of the equilibrium range when $1.5 < f/f_p < 2.1$, there is less symmetry in the directional distributions. A more dramatic variation occurs at the directional peaks, with some directional peaks aligned with the wind (Figs. 2h and 2m) and some peaks deviating from the wind direction by 50°–60° (Figs. 2b and 2p). The sequence of spectra in Figs. 2h–o suggests a strong influence on fetch. In Fig. 2m, the wind comes from the long-fetch opening at the south end of the sound (Fig. 1), the directional distribution peak is near the wind direction, and the directional distribution function is approximately symmetric about the wind direction. Figures 2l and 2n show wind direction classes that are 20° on either side of results shown in Fig. 2m. Figures 2k and 2o, in direction classes that are 40° away from the class in Fig. 2m, have directional peaks shifted 40° from the wind direction, toward the long-fetch direction.

b. Hurricane Wilma

Hurricane Wilma propagated from the Yucatan Peninsula on a storm track that was oriented to the northeast. It propagated over Florida and then continued to move toward the northeast, parallel to the coast as shown in Fig. 3. Although its central sea level pressure reached a record 896 hPa while in the Gulf of Mexico, exceeding

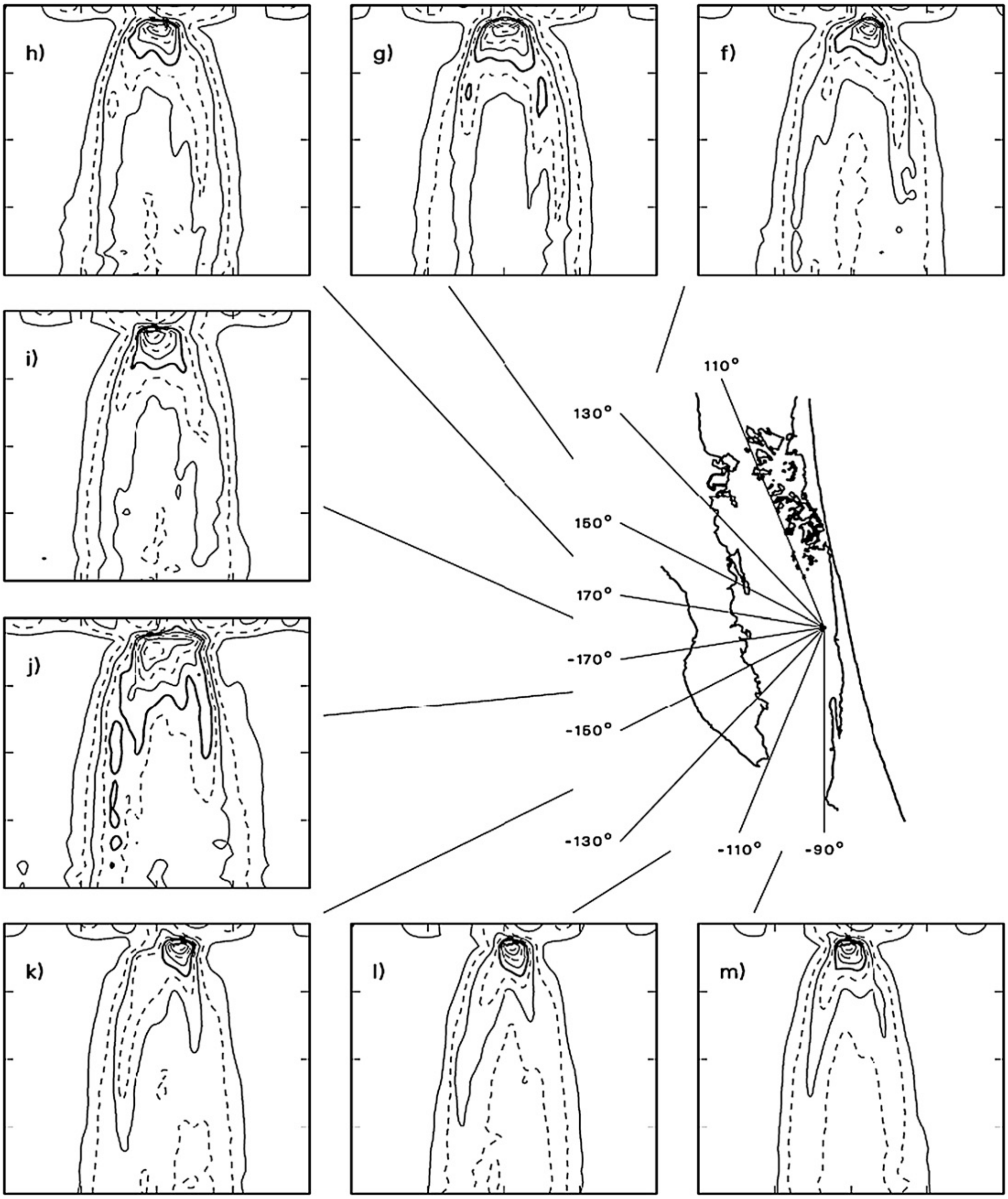

FIG. 2. Contour plots of the directional distributions for composite spectra from Long and Resio (2007). In this paper, we focus on classes c, i, k, and o. Contours are at tenths of the directional distribution maximum in each plot. Class o, with winds 40° positive from class m, has a peak direction about 40° negative to the wind, which aligns with the long fetch of class m.

category 5 storm intensity, it had weakened considerably by the time it passed by Cape Hatteras. Maximum winds recorded at the directional waverider (630 in Fig. 1) near the Field Research Facility reached 14.6 m s^{-1}, and maximum significant waves were 4.13 m at 2200 eastern standard time (EST) 24 October 2005.

Wave buoy 630 is a standard Datawell directional waverider, from which synoptic time series of heave, surge, and sway are collected in 4096-point records at 1.28 Hz, or about 53 min in duration. Fourier analysis of these records with segment and band averaging yields auto- and cross-spectral estimates having 48 degrees of freedom in bands of 0.0075-Hz width. A directional distribution function is estimated for each frequency band using the conventional truncated Fourier series method of Longuet-Higgins et al. (1963). The resulting

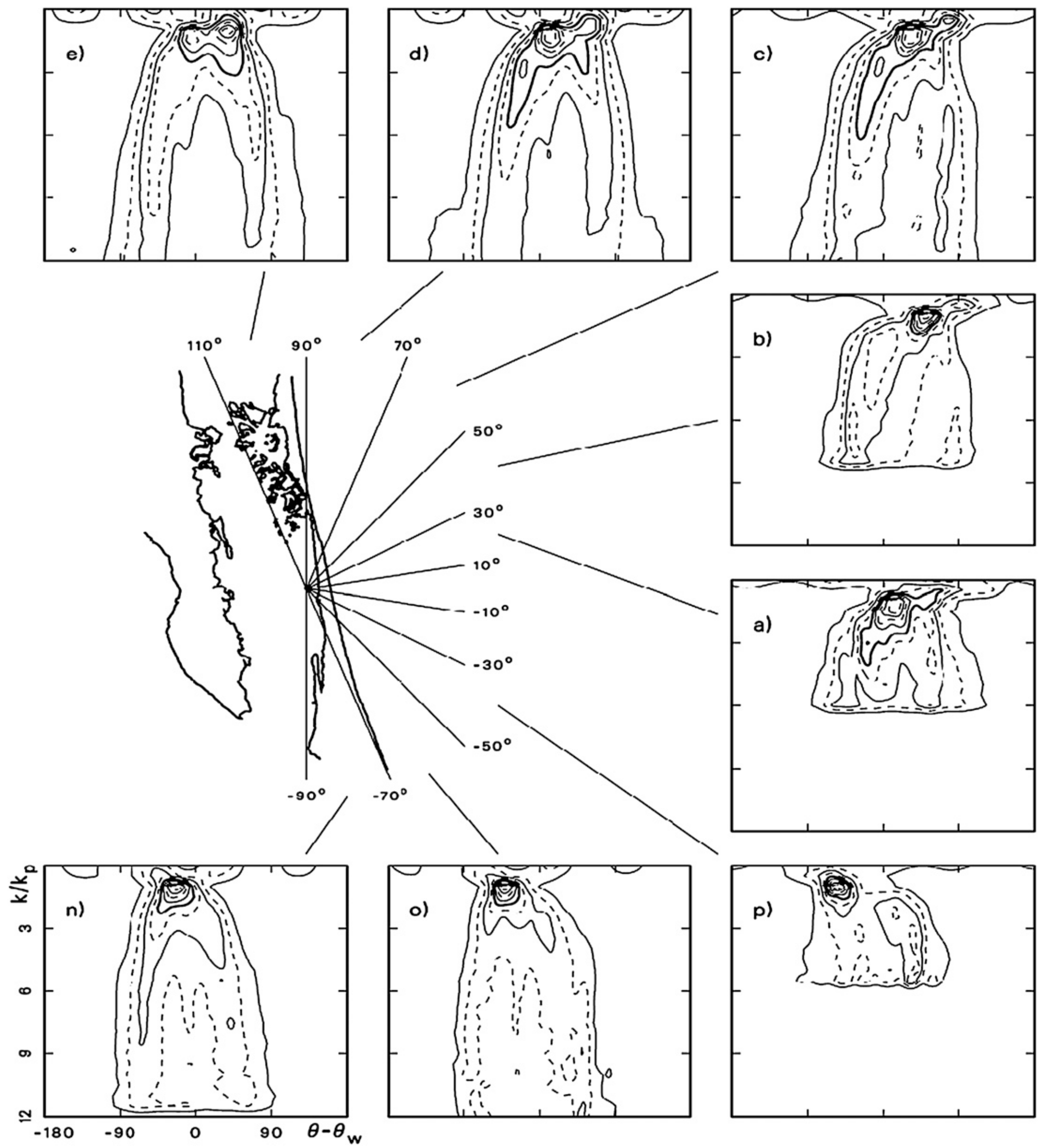

FIG. 2. (*Continued*)

spectra have 85 linearly spaced bands from 0.005 to 0.635 Hz.

Much of the buoy data consist of complicated mixed seas. We focus on the waves at the peak of the storm during the period from 0700 EST 24 October to 0700 EST 25 October, as wind-generated waves from Wilma grow to their maximum values and then decay as the storm moves past Cape Hatteras and the wave spectra exhibit directional shear. During this time, the peak spectral wave direction is approximately constant with an average direction of about 45°–65°, whereas the wind direction changes continuously, ranging from 79° to 295°. The average change in wind direction was about 3° h^{-1}; the maximum wind direction change was about 25° h^{-1}, occurring at 0100 EST 25 October.

c. Data preparation

To make comparisons among the three S_{nl} formulations (DIA, TSA, FBI), the observed directional wave spectra are converted from a linearly spaced grid to a coordinate system with radial logarithmically spaced coordinates, following Part I, so that for any geometrically similar coordinates, the locus equation for the nonlinear four-wave interactions also scales linearly. This conversion is achieved by linear interpolation of the spectra from the linear grid described in section 2b to

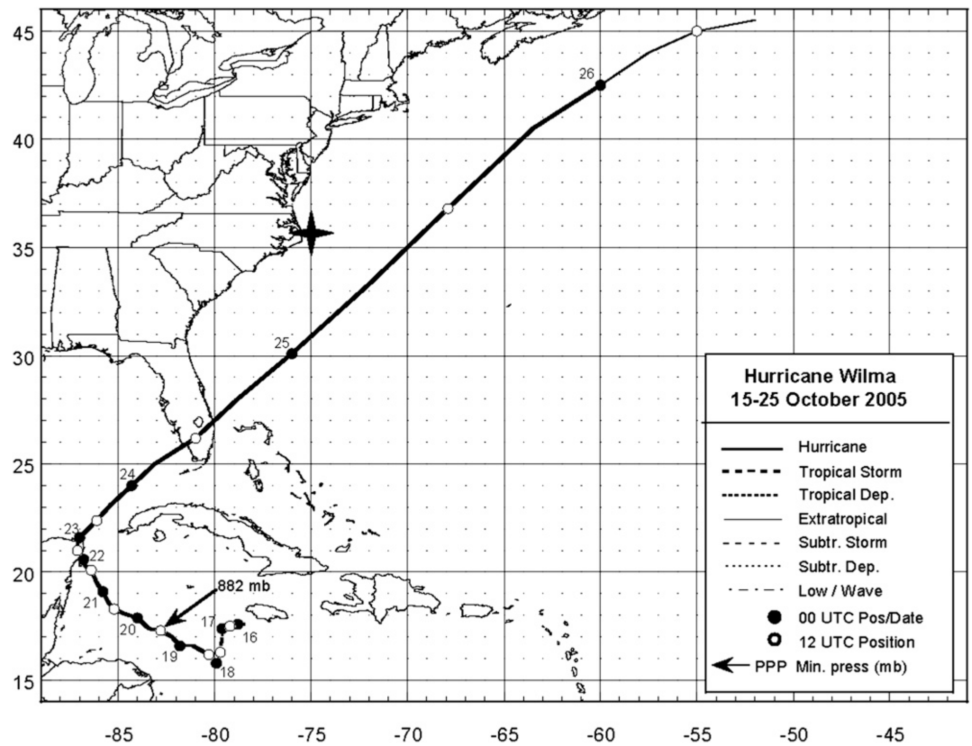

FIG. 3. Best-track positions for Hurricane Wilma, October 2005. Track during the extratropical stage is partially based on analyses from the National Oceanographic and Atmospheric Administration Ocean Prediction Center. (Available online at http://www.nhc.noaa.gov/2005atlan.shtml.) FRF is indicated by the large four-pointed star.

the logarithmically spaced grid described in Part I. The latter is constructed by specifying a number of bins for the forward face ($f/f_p < 1.0$) of the spectrum and by matching the spectral peak with a particular grid point. For example, if 13 bins are desired in the spectral forward face, then the logarithmically spaced frequency coordinates are defined as

$$f_m = f_p \lambda^{m-14}, \tag{5}$$

where f_p is the peak frequency, m is the radial coordinate index, and λ is a constant greater than unity, such as 1.1.

3. Comparisons of S_{nl} estimates for Currituck Sound data

We present detailed comparisons of the three S_{nl} formulations (DIA, TSA, and FBI) for four selected examples from the Currituck wave dataset. These are indicated as classes c, i, k, and o in Fig. 2. These classes are selected because they provide differing growing-fetch and slanting-fetch wind-generated wave spectra and wave ages. Additional comparisons including all classes of the Currituck dataset are presented in section 3d.

Class i corresponds to shore-normal winds from the west and a directional distribution that is approximately symmetric about the mean wind direction, with the directional peak aligned with the wind. Class c is a slanting-fetch case with winds from the northeast and the spectral peak deviating from the wind direction by about 50°–60°. Class k corresponds to a directional distribution that is approximately symmetric about the mean wind direction for $k/k_p > 2.1$, with the mean wave direction tending to align with the wind direction. However, for the lower part of the equilibrium range ($1.5 < k/k_p < 2.1$), there is less symmetry in the directional distributions and the directional peaks are dramatically misaligned, with the wind deviating by about 25°–50°. Fetch is a strong influence on classes i, k, and o. In class o, the dominant direction is 40° away from that of class m, which is along the long-fetch opening at the south of the sound, and the directional peak is shifted 40° from the wind direction, toward the long-fetch direction.

a. *Currituck 1D cases and TSA decomposition functions*

As presented in Part I and discussed in the introduction, the general approach followed in the TSA

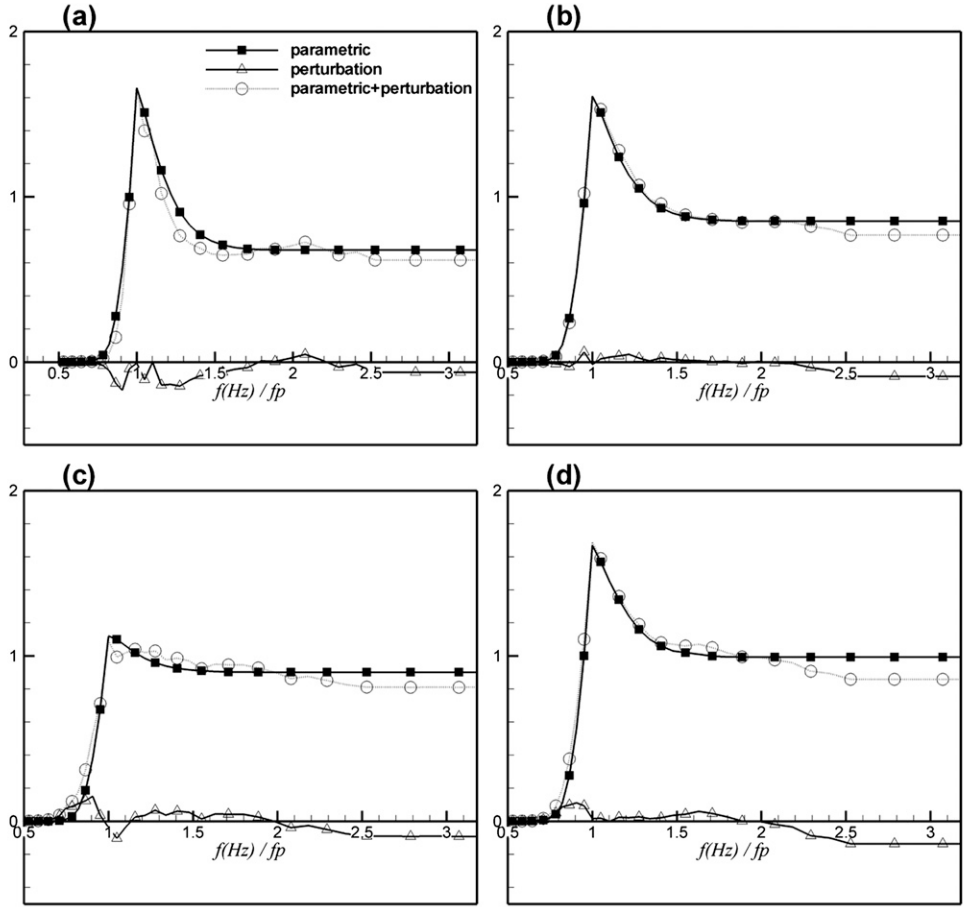

FIG. 4. The 1D energy decompositions for construction of TSA for selected Currituck wave spectral cases: (a) class i, (b) class k, (c) class o, and (d) class c from Fig. 2. Each panel shows the parametric term, the perturbation function, and the corresponding 1D energy spectrum (parametric + perturbation). These terms are normalized by ω^4, as representative of the functional variation of the equilibrium range, and in the frequency coordinate by the spectral peak frequency f_p.

implementation is first to decompose a given directional spectrum into a parametric spectrum and a residual nonparametric component. The inclusion of the residual component allows this decomposition to retain the same number of degrees of freedom as the modeled spectrum. This decomposition leads to a representation of the interactions in terms of broad-scale interactions, local-scale interactions, and interactions between the broad-scale and local-scale components of the spectrum. This approach allows the broad-scale interactions and certain portions of the local-scale interactions to be precomputed.

Figures 4a–4d present the 1D energy density decompositions of the four Currituck spectral examples mentioned in the previous section. These plots show that in each of the four selected Currituck cases the parametric terms exhibit the main behavior of the spectra. The consequent perturbation functions provide the additional degrees of freedom necessary to represent the spectra. Thus, in each case it is expected that the TSA will have good ability to capture a reasonable representation of the nonlinear interactions for these spectra. The 1D spectra portrayed in Figs. 4a, 4b, and 4d are similar in terms of the ability of the decompositions to capture the characteristics of the energy densities. Figure 4c is different because the spectral peak is largely absent because of the shear from the slanting geometry, which is the prominent feature of this particular class. The associated TSA representations of the nonlinear transfer are shown in Figs. 5a–d.

Figures 5a–d show several similar characteristics. In each case it is evident that the nonlinear transfer resulting from broad-scale (parametric) contributions does not accurately represent the nonlinear transfer, as suggested by the FBI. For each of the spectra, the TSA and FBI compare well for the forward face ($f/f_p < 1.0$)

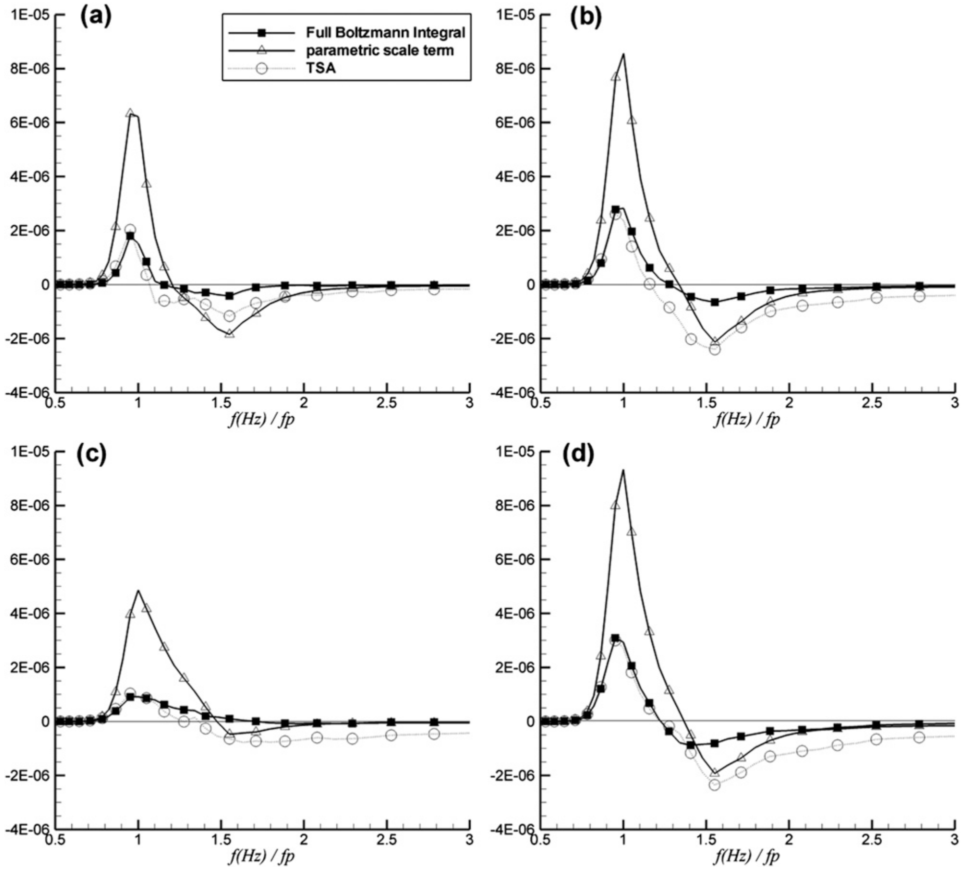

FIG. 5. The 1D energy transfers from the TSA and FBI formulations corresponding to Figs. 4a–d. Units for the y axis: m^2 Hz^{-1} s^{-1}. In this and subsequent figures, a label value of E$-$XX indicates multiplication by 10^{-XX}.

and spectral peak regions. Thereafter, for the rear face ($1 < f/f_p < 1.5$) and in the equilibrium range ($1.5 < f/f_p < 3.0$), the TSA tends to overestimate the negative transfer rate of the FBI. However, the TSA achieves good overall agreement with the variations of the FBI, as a function of normalized frequency f/f_p, where f_p is the peak frequency. We note that the x axis in Figs. 5a–d is truncated to show the details of the nonlinear transfer around the spectral peak and that the FBI and TSA formulations do indeed conserve energy, despite the portion of their plots given in these figures.

The relatively poor agreement between transfer rates estimated by the parametric (broad scale) component of the TSA and the FBI seems initially a bit surprising, given the good fit between the parametric spectra and the actual measured spectra shown in Fig. 4. However, it should be recognized that the degree of agreement shown in Fig. 4 is only for the directionally integrated spectra. The version of the parametric functions used here to capture the broad-scale energy variation assumes a constant directional spreading [of $\cos^{2s}(\theta - \theta_p)$ form] relative to the peak direction θ_p. As shown in Fig. 2, the angular distributions of energy in the Currituck data vary strongly near the peak and do not closely follow the $\cos^{2s}(\theta - \theta_p)$ form. To test the hypothesis that it is indeed the variation in angular spreading that is responsible for a substantial portion of the deviations seen in Fig. 5, we altered the input spectrum, giving it a constant angular spreading of $\cos^6(\theta - \theta_p)$, while maintaining the same directionally integrated shape. Figure 6 shows the results for this case. Figure 6a gives the decomposition of the spectrum of Fig. 4a using a constant $\cos^6(\theta - \theta_p)$ angular spreading, showing that the parametric term gives the main behavior and the perturbation function provides additional degrees of freedom needed to represent the spectrum. Figure 6b gives the resulting 1D nonlinear spectral transfers from the TSA and FBI. In this case the parametric scale component of the TSA is evidently in much better agreement with the FBI than is achieved in Fig. 5a.

The results shown in Figs. 5 and 6 represent an important distinction from the tests shown in Part I in

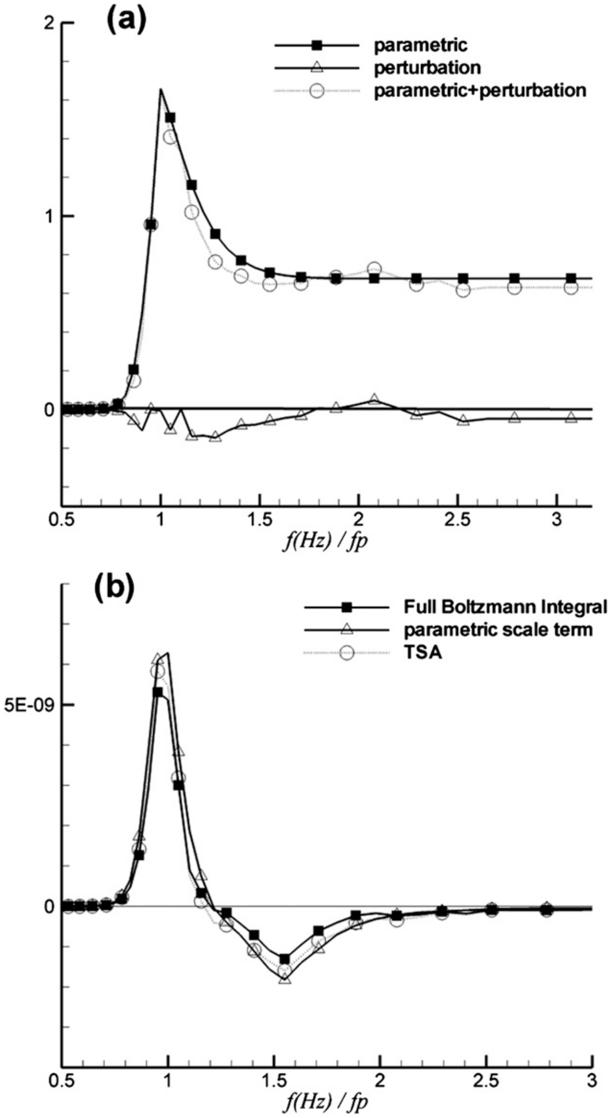

FIG. 6. (a) Decomposition of the spectrum of Fig. 4a using a constant $\cos^6$ angular spreading, showing the parametric and the perturbation functions. As in Fig. 4, the parametric term, the perturbation function, and the 1D energy spectrum are normalized by ω^4 and in the frequency coordinate by the spectral peak frequency f_p. (b) Corresponding 1D transfer with TSA and FBI. Units: $m^2\ Hz^{-1}\ s^{-1}$.

which the angular spreading was held constant. Two very important points can be drawn from Figs. 5 and 6. First, variations in directional spreading can significantly affect nonlinear transfer rates; thus, it is critical that operational approximations to the full integral properly capture the directional attributes of the nonlinear fluxes to model wave evolution properly. Second, the perturbation-scale term in the TSA is absolutely critical to the representation of nonlinear transfers in observed spectra since it is highly unlikely that the broad-scale parameterization can capture all of the important nuances of the spectral shape, which can affect the nonlinear transfer rates.

b. Comparisons in 1D of nonlinear transfer between TSA and DIA

Figures 7a–d compare the 1D nonlinear transfer rates for the four Currituck spectral examples discussed in the previous section, using the three S_{nl} formulations. The comparison is notable for several considerations. In each case, on the spectral forward face, the DIA approximately achieves some ability to compare with the FBI results, albeit with varying degrees of difficulty. By comparison, the FBI and TSA results agree relatively well on the forward face. On the rear face of the spectrum, in each of the four spectral examples, the DIA appears to be erratic and performs poorly relative to the TSA, and the TSA suggests a transfer rate that has a negative bias in comparison with the FBI. In the equilibrium range, the DIA compares more closely in magnitude to the FBI than does the TSA but tends to have erratic tendencies, whereas the TSA and the FBI appear to correlate well.

Systematically these results show that the TSA gives results that retain many of the FBI characteristics, with similar values and smooth behavior. By comparison, the DIA results appear erratic and tend to show large differences in comparison with the FBI results.

c. Comparisons in 2D nonlinear transfer cases between TSA and DIA

Detailed 2D comparisons are displayed in Figs. 8a–d, for each of the four Currituck spectral examples in Figs. 5 and 7. These results show that the TSA and the FBI compare relatively well, qualitatively and quantitatively. Each display has similar gross features in terms of the forward face, the rear face, the equilibrium range, and the directional spectral distributions associated with these regions. Overall, both the FBI and the TSA appear to be well behaved, with little indication of spectral noise or instability. Qualitatively, symmetric and asymmetric spectral features are generally reflected in the resulting transfer rates suggested by the FBI and the TSA. For example, both the TSA and the FBI display regions of negative transfer rates in the spectral rear-face region, with some secondary asymmetries reflecting asymmetric features in the 2D wave spectra. At high frequencies, both display regions of slightly negative transfer rates reflecting the associated bimodal regions in the 2D spectra, as noted in Fig. 2.

In contrast to the TSA results, the DIA compares poorly with the FBI. Although the DIA suggests positive and negative regions of transfer rates, these regions

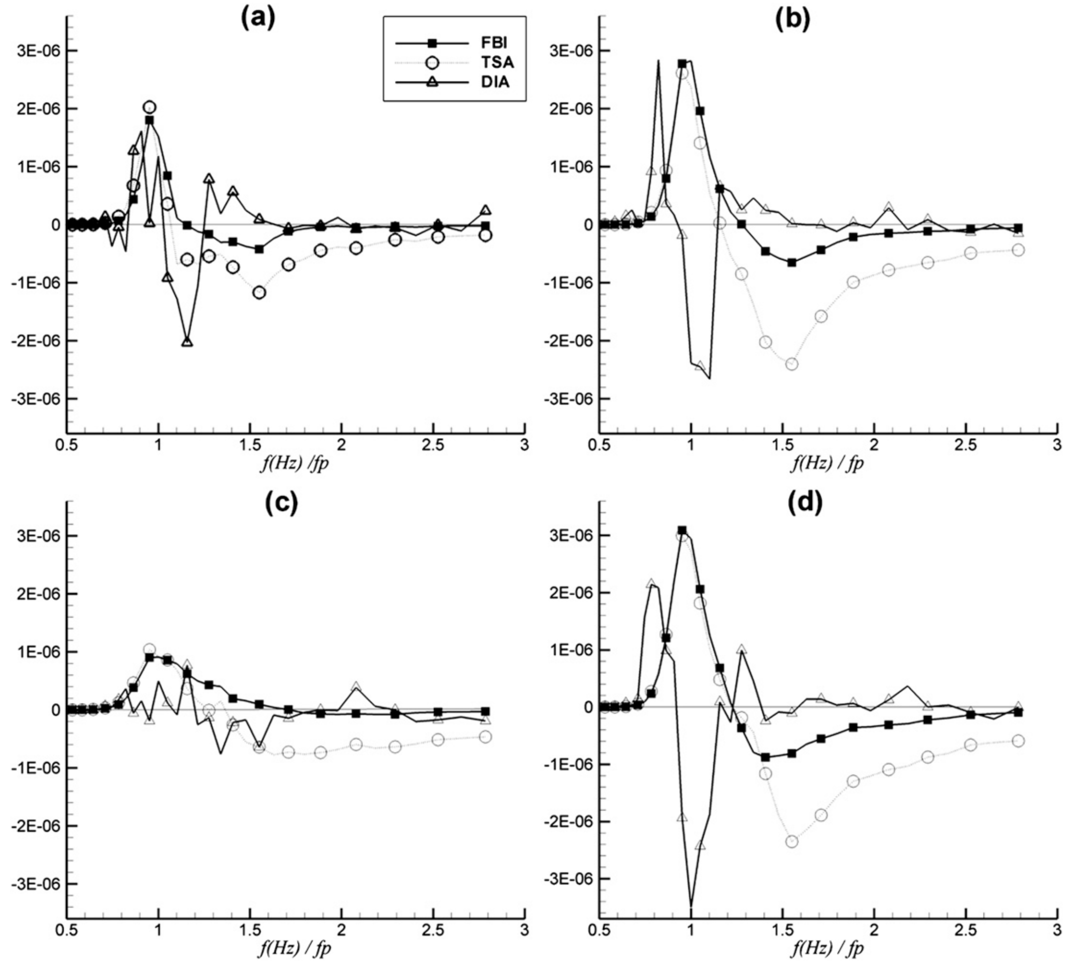

FIG. 7. Comparisons of 1D nonlinear transfer (m^2 Hz^{-1} s^{-1}) for FBI, TSA, and DIA using Currituck Sound data for (a) class i, located west (from $-170°$ to 170°) from the wave-staff array sled; (b) class k, located west (from $-110°$ to $-130°$) from the sled; (c) class o, located west (from $-70°$ to $-90°$) from the sled; and (d) class c, located west (from $+50°$ to $+70°$) from the sled.

appear to be haphazard, with incorrect magnitudes, poor estimates of locations of regions of positive and negative transfer rates in the 2D domain, and incorrect shapes and spectral distributions. Qualitative features are sufficiently dissimilar, in comparison with the FBI, that differences are qualitatively large. Overall, the DIA results appear to be erratic and exhibit little similarity with 2D distributions of the FBI results.

d. Statistical comparisons between TSA and DIA

In Figs. 9a–c, we give the normalized root-mean-square errors (NRMSE) and correlation coefficients for all of the 1D Currituck Sound spectral cases, for the TSA and DIA formulations, with respect to the FBI. The normalization of the NRMSE is obtained by dividing RMSE by the full range of the FBI values, $|\max(S_{nl}) - \min(S_{nl})|$. Results for all of the Currituck spectra, computed for the entire 1D spectrum, show that NRMSE values computed for the TSA are about one-half of those resulting for the DIA. Clearly, different regions of the spectra respond differently. Figures 9a and 9b suggest that, for the forward face, the TSA achieves NRMSE values that are about one-fifth of the DIA NRMSE values. For the rear face, NRMSE values for the TSA are only about one-half of those of the DIA. In the equilibrium range, NRMSE values for the TSA are similar to those of the DIA.

Correlation coefficients are given in Fig. 9c for the TSA and DIA results in comparison with those of the FBI. These computations are with respect to the complete 1D Currituck spectral cases, as well as for the spectral regions (forward face, rear face, and equilibrium region) within the 1D spectra. Results for the TSA are notable. For the 1D Currituck Sound spectral cases, correlation coefficients for the TSA relative to the FBI are nearly unity, computed for the entire spectral range. Moreover, for specific regions such as forward-face, rear-face, and equilibrium-range regions, correlation coefficients for the TSA relative to the FBI are near unity. By comparison, correlation coefficients for the DIA relative to the FBI are about 0.5 for the entire spectral range. For the forward-face regions the correlation coefficients of the DIA results relative to the FBI vary from about −0.5 to about 1.0. These values decline to varying from about −0.2 to 0.7 for the rear-face regions of these spectra and to varying from −1.0 to 0.5 for the equilibrium-range regions.

4. Comparisons of S_{nl} estimates for Hurricane Wilma wave data

This section presents comparisons of the three S_{nl} formulations using directional waverider wave spectra data collected during Hurricane Wilma (Fig. 3), as the waves grow to their maxima and then decay as the storm moved beyond Cape Hatteras. The wave buoy was moored off the Field Research Facility at Duck. Statistical comparisons for all spectra collected from 0700 EST 24 October until 0700 EST 25 October are also given.

Wave spectra from four cases from Hurricane Wilma are displayed in Figs. 10a–d. These cases represent conditions in which waves grow and then decay: (a) 1300 EST 24 October soon after Wilma emerged from crossing Florida and began propagating northeastward along a storm track typical of North Atlantic hurricanes, (b) 2200 EST 24 October as waves achieve their peak at the waverider, (c) 0100 EST 25 October as the hurricane passes the Field Research Facility and waves begin to decay and the spectrum shows shear in its equilibrium range, and (d) 0700 EST 25 October as the waves have significantly decayed and directional shear is pronounced. Details of the significant wave heights, wind speed U_{10}, peak wave direction θ_p, and wind direction θ_{10} appear in Table 1. The wave spectrum at 1300 EST 24 October (Fig. 10a) appears to be symmetric and does not show evidence of shear. As the waves reach their peak at 2200 EST 24 October (Fig. 10b), some high-frequency spectral shearing is evident, modulating the overall symmetric structure. In the storm's decay phase, at 0100 and 0700 EST 25 October (Figs. 10c and 10d), the spectra become asymmetric.

a. *TSA decomposition functions for Hurricane Wilma spectra*

As in the discussion of the Currituck spectral classes, we first consider the TSA in terms of the decomposition of directional spectra into parametric spectral functions and associated residual nonparametric components. For wave conditions generated by Hurricane Wilma, does the decomposition formulation allow a reasonable representation of the observed field spectra? If the residual nonparametric components are large relative to the parametric spectral functions, how well do results from the TSA compare to the FBI?

Figures 11a–d present the 1D energy density decompositions for the four waverider wave spectral examples shown in Figs. 10a–d. These plots show that, in these cases of growing waves and changing wind conditions, there is good ability of the decomposition to capture a reasonable representation of the spectra, even for the fourth case (0700 EST 25 October), when the spectra are highly sheared. In each of these cases, the parametric terms give the main behavior of the spectra and the perturbation functions provide the necessary additional degrees of freedom to represent the spectra.

The 1D spectra in Figs. 11a and 11b are similar, and the decompositions approximately capture the behavior of the observed energy densities. Figure 11c differs from Figs. 11a and 11b in that shear is beginning to occur and the spectral peak is largely absent because of the rapidly changing wind directions, which dominate the spectral wave development. The fourth case (Fig. 11d) depicts a frequency spectrum that is directionally sheared. Although the parametric function is able to represent the spectral peak and rear-face regions, it fails to follow the complete behavior for the upper-frequency region of the observed equilibrium range. In this highly sheared portion of the equilibrium range, the parametric function exhibits a departure from the measured data.

The corresponding TSA results for nonlinear transfer are shown in Figs. 12a–d, for the spectral cases shown in Figs. 11a–d. Several similar characteristics are evident in these plots. In cases of growing waves (with no shear) in Figs. 12a and 12b, the parametric scale term and the resulting TSA are similar. Both significantly overestimate the transfer rates on the forward face of the spectrum and at the spectral peak, in comparison with the FBI. Both approximately capture the FBI behavior in the rear-face and equilibrium-range regions of the spectrum. Both correlate relatively well with the variations of the FBI over the entire spectrum.

Figure 12c is different from Figs. 12a and 12b, because shear is beginning to be felt in the high-frequency portion of the equilibrium region in this case. Consequently, both the parametric scale term and the resulting TSA can largely simulate the FBI behavior on the forward face of the spectrum and the spectral peak region, with some overestimate in values, as in Figs. 12a and 12b. However, divergence becomes noticeable for the equilibrium range and tends to grow for increasing frequencies as one moves to the high-frequency portion of the

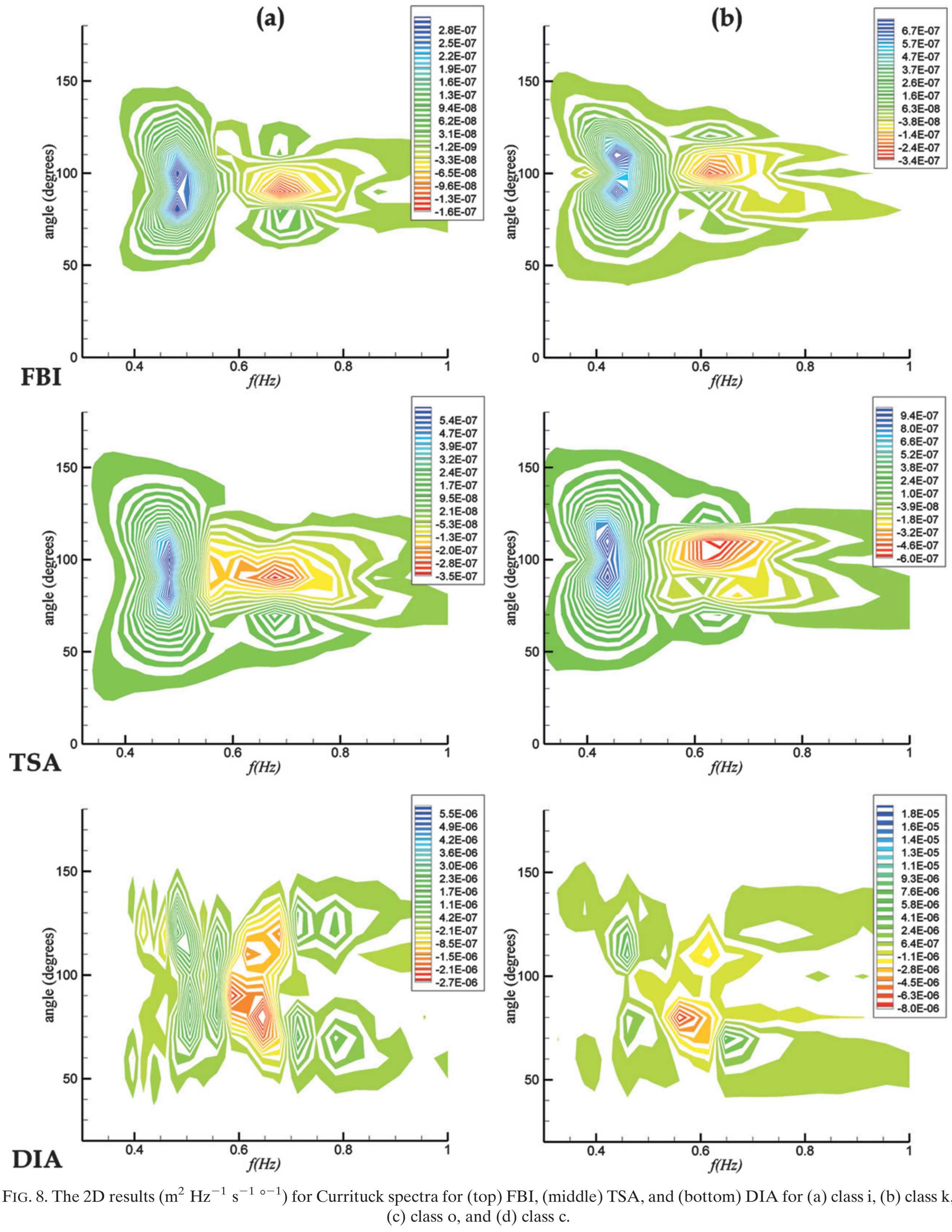

FIG. 8. The 2D results ($m^2\ Hz^{-1}\ s^{-1}\ {}^{\circ -1}$) for Currituck spectra for (top) FBI, (middle) TSA, and (bottom) DIA for (a) class i, (b) class k, (c) class o, and (d) class c.

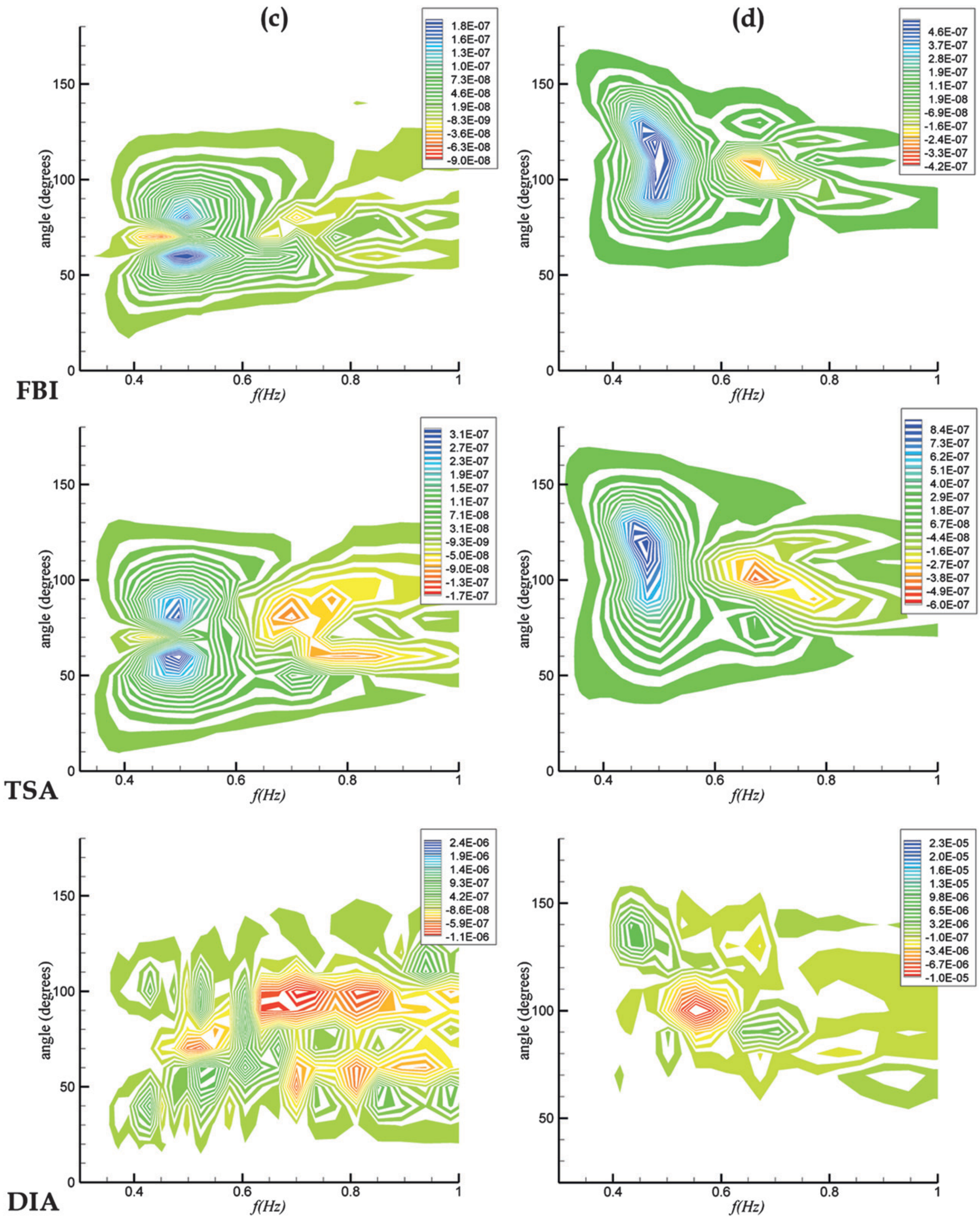

FIG. 8. (*Continued*)

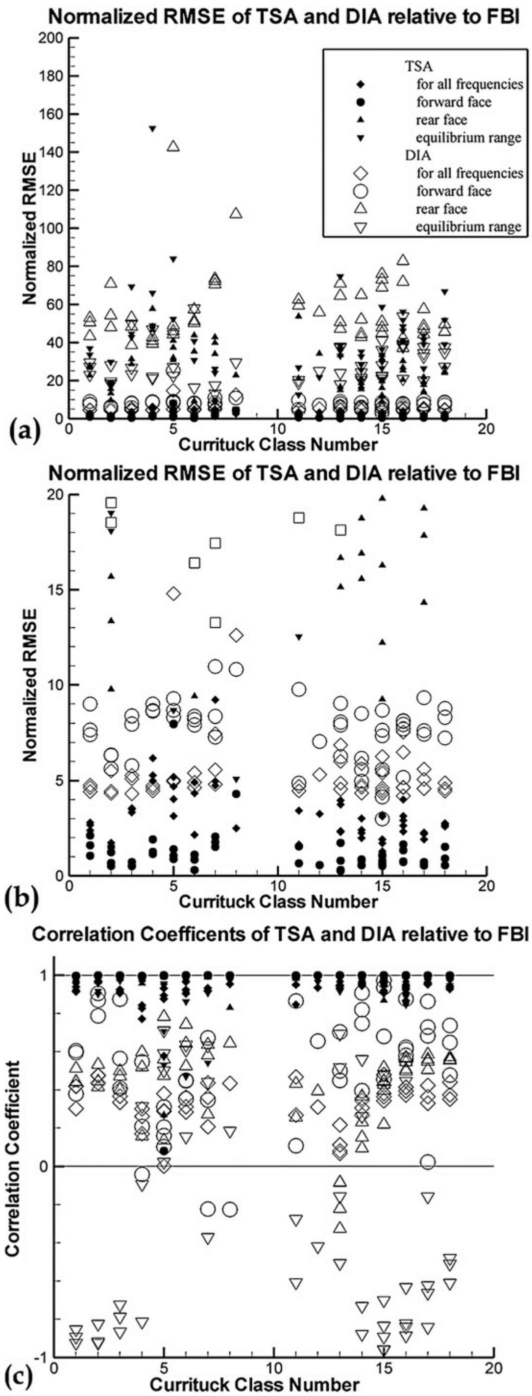

FIG. 9. (a) Error calculations showing NRMSE of TSA and DIA relative to FBI for all Currituck spectra cases; (b) blown-up image of lowest part of (a). Cases are numbered sequentially according to angular bins in Fig. 2 and inverse wave ages U_{10}/C_p, starting with the angular bin [170.0°, −170.0°] and $1.5 < U_{10}/C_p < 2.0$, increasing in U_{10}/C_p bins, and then moving counterclockwise to the next angular bin [−170.0°, −150.0°], and continuing for all Currituck cases. (c) Error calculations for all Currituck spectra cases showing correlation coefficients.

equilibrium range, reflecting increasing shear. In a more demanding test, Fig. 12d gives the results corresponding to the highly sheared spectrum in Fig. 11d. In this case, the parametric scale term and the resulting TSA can simulate the forward-face and rear-face regions of the FBI. Although the TSA and the FBI remain comparable in the equilibrium range, they tend to diverge with increasing frequency values.

b. Comparisons in 1D nonlinear transfer cases between TSA and DIA

Figures 13a–d compare the 1D nonlinear transfer rates for the four spectral cases discussed in Figs. 11 and 12, using the three formulations. Several overall trends are evident. In the cases of growing waves in Figs. 13a and 13b, the TSA overestimates the FBI on the forward-face and spectral peak regions and otherwise behaves comparably, correlating well with the FBI characteristics. In particular, the TSA approximately captures the FBI behavior in the rear-face and equilibrium-range regions of the spectrum. By comparison, the DIA achieves only a very loose approximation to the FBI behavior for all of these regions, for the forward face, rear face, and equilibrium range, and appears to be chaotic.

Results suggested in Figs. 13a and 13b are also evident in Fig. 13c; high-frequency shear in the spectrum gives additional effects. Figure 13c shows that the TSA can largely simulate the FBI behavior on the spectral forward face although divergence between the two formulations becomes noticeable and tends to grow for increasing frequencies in the equilibrium range (as suggested in Fig. 12c). By comparison the DIA gives poor results, with only a rough qualitative approximation to the FBI behavior in all regions of the spectrum. Figure 13d gives the comparisons for the highly sheared spectrum (following Figs. 11d and 12d), showing that in this case the TSA can simulate the FBI well, for the forward- and rear-face regions of the spectrum, with increasing divergence from the FBI occurring for increasing frequencies in the equilibrium range. By comparison, the DIA fails to capture the main FBI variations for the forward-face or rear-face regions and diverges significantly in the equilibrium range.

In all four cases, the FBI and TSA results appear to be similar and agree relatively well, whereas the DIA performs relatively poorly. The TSA is somewhat biased in magnitude relative to the FBI, although these two formulations tend to have highly correlated variations, with respect to the frequency axis, whereas the DIA appears chaotic. Overall, the TSA shares many characteristics with the FBI, with relatively similar values and smooth behavior, whereas the DIA appears to be erratic and differs significantly from the FBI.

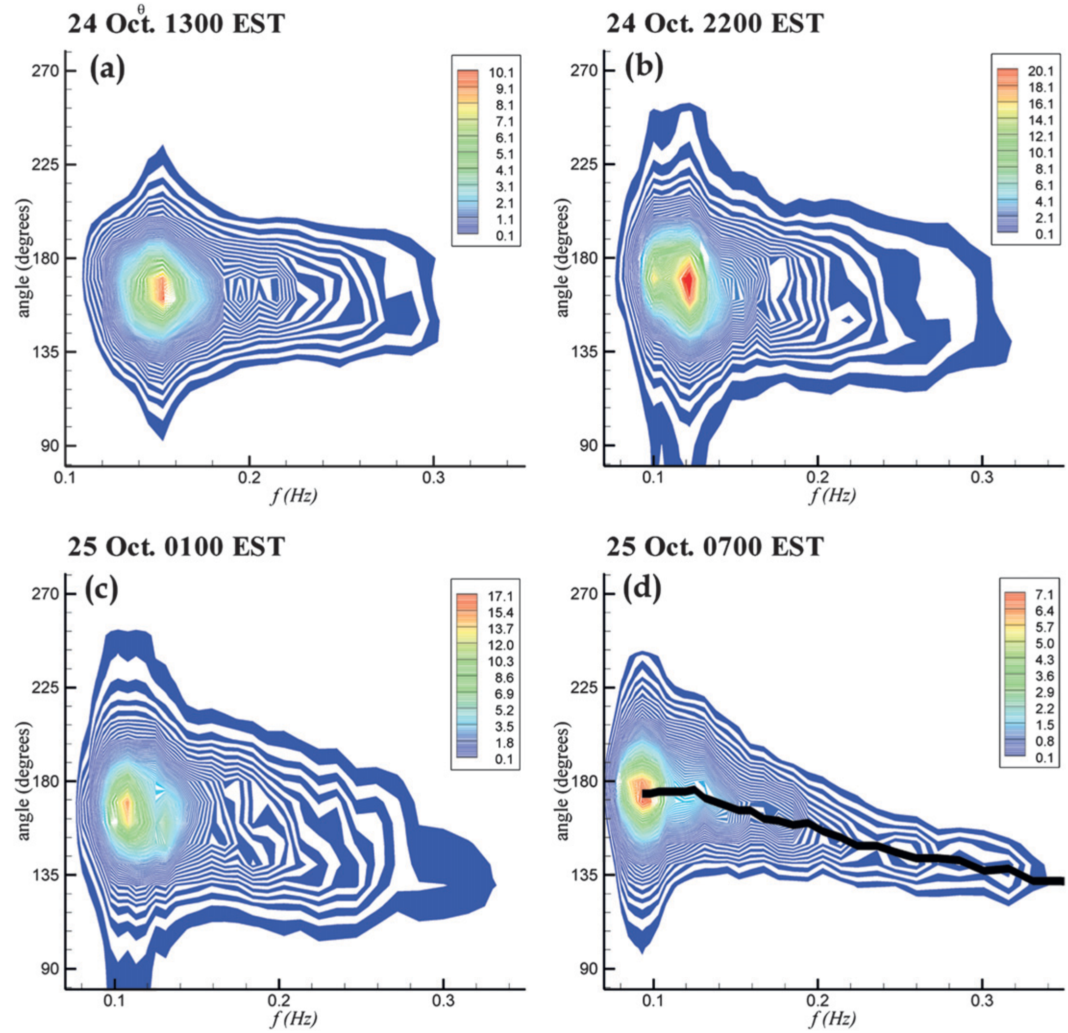

FIG. 10. Two-dimensional wave spectra (m^2 Hz^{-1} s^{-1} $^{\circ -1}$) observed by the directional waverider moored off Duck, NC, during Hurricane Wilma (time and date indicated in each panel), for different spectra, wind direction θ_{10}, and peak wave directions θ_p: (a) developing wind-sea spectra; (b) peak spectra, winds almost collinear with peak wave direction, sheared tail; (c) decreasing sheared spectra; and (d) decreasing directionally sheared frequency spectrum. The solid black line in (d) indicates the mean wave direction plotted as a function of frequency.

c. Comparisons in 2D nonlinear transfer

Detailed 2D results are displayed in Figs. 14a–d, comparing the three formulations, for the four spectral examples considered in Fig. 10. Overall, these results show that directional distributions of the TSA and the FBI compare relatively well, qualitatively and quantitatively, displaying similar gross features for the forward-face, the rear-face, and the equilibrium-range regions of the spectrum. There are differences between the TSA

TABLE 1. Characteristics of wave spectra shown in Figs. 10a–d, showing significant wave heights (Hs), wind speed U_{10}, peak wave direction θ_p, and wind direction θ_{10}.

Fig.	Time (EST) and date	Hs (m)	U_{10} (m s^{-1})	θ_p (°)	θ_{10} (°)	$\theta_p - \theta_{10}$ (°)
10a	1300 24 Oct	2.68	12.9	69.86	76.33	−6.47
10b	2200 24 Oct	4.13	12.3	55.86	17.35	+38.51
10c	0100 25 Oct	3.57	13.9	53.86	347.71	+66.15
10d	0700 25 Oct	2.45	9.6	49.86	294.53	+115.33

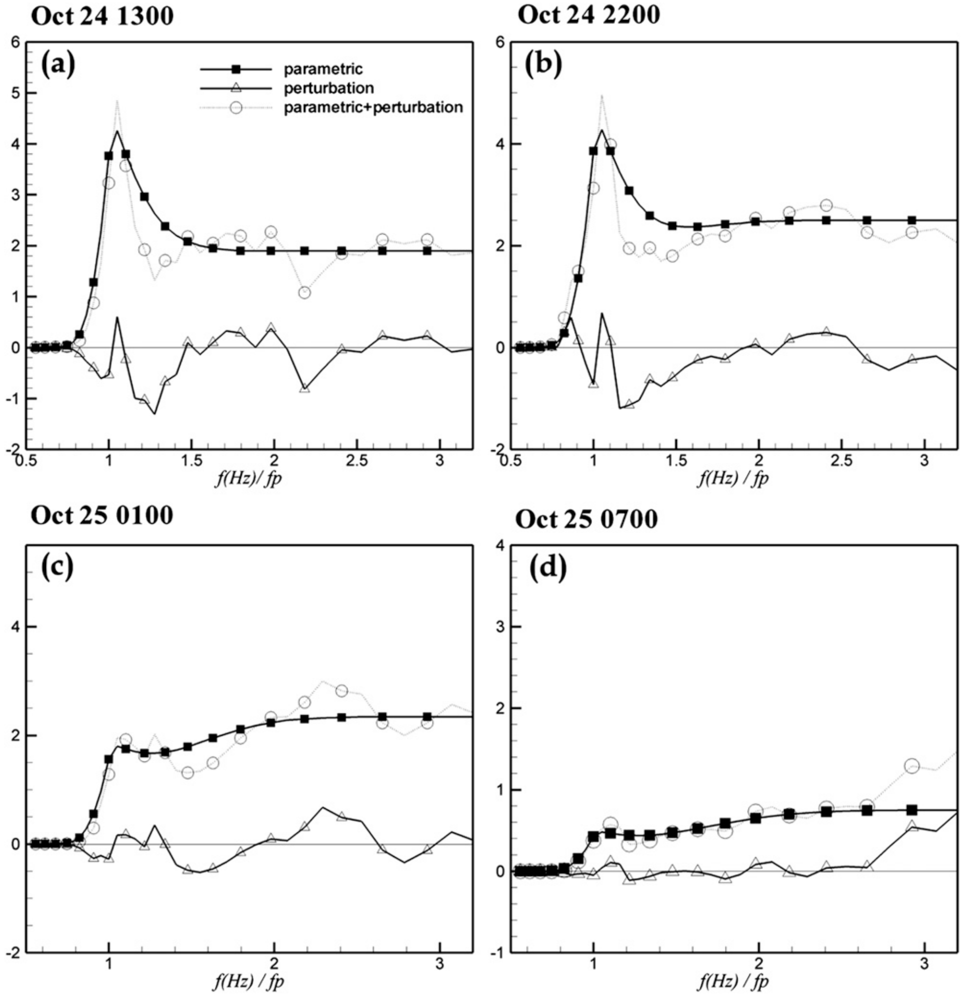

FIG. 11. The 1D energy decompositions for construction of TSA for four selected waverider spectra during Hurricane Wilma showing parametric terms, perturbation functions, and the corresponding 1D energy spectrum (parametric + perturbation). As in Fig. 4, these terms are normalized by ω^4 in each case and by the spectral peak frequency f_p in the frequency coordinate.

transfer rates in comparison with those of the FBI for positive and negative transfer rate regions of the spectrum. Qualitatively, features suggesting symmetric and asymmetric spectral characteristics are generally reflected in the transfer rates estimated by the FBI and TSA with little indication of chaotic behavior. Both display shear effects (in Figs. 14c and 14d) reflecting the sheared input 2D spectra.

Results in 2D for the DIA compare poorly to the FBI. Although the DIA achieves some positive and negative regions of transfer rates, these regions appear to be haphazard, with incorrect magnitudes and poor estimates of locations of regions of positive and negative transfer rates in the 2D domain, and have incorrect shapes and spectral distributions in comparison with the FBI. The DIA does not exhibit important regions of positive transfer rates, as compared with the TSA and FBI. Qualitative features are dissimilar in comparison with the FBI, and differences are qualitatively large. Overall, the DIA appears to exhibit little similarity with the FBI distributions.

d. *Statistical comparisons between TSA and DIA*

Estimated NRMSEs and correlation coefficients for all Hurricane Wilma spectra during the period from 0700 EST 24 October until 0700 EST 25 October are given in Figs. 15a–c, comparing the TSA and DIA with the FBI. As an overall result computed for the entire spectrum, values for NRMSE computed for the TSA are about one-half of those resulting for the DIA (Fig. 15b). Figures 15a and 15b suggest that over specific spectral regions (e.g., forward face, rear face, and equilibrium range) NRMSE values for the TSA also appear to be approximately on

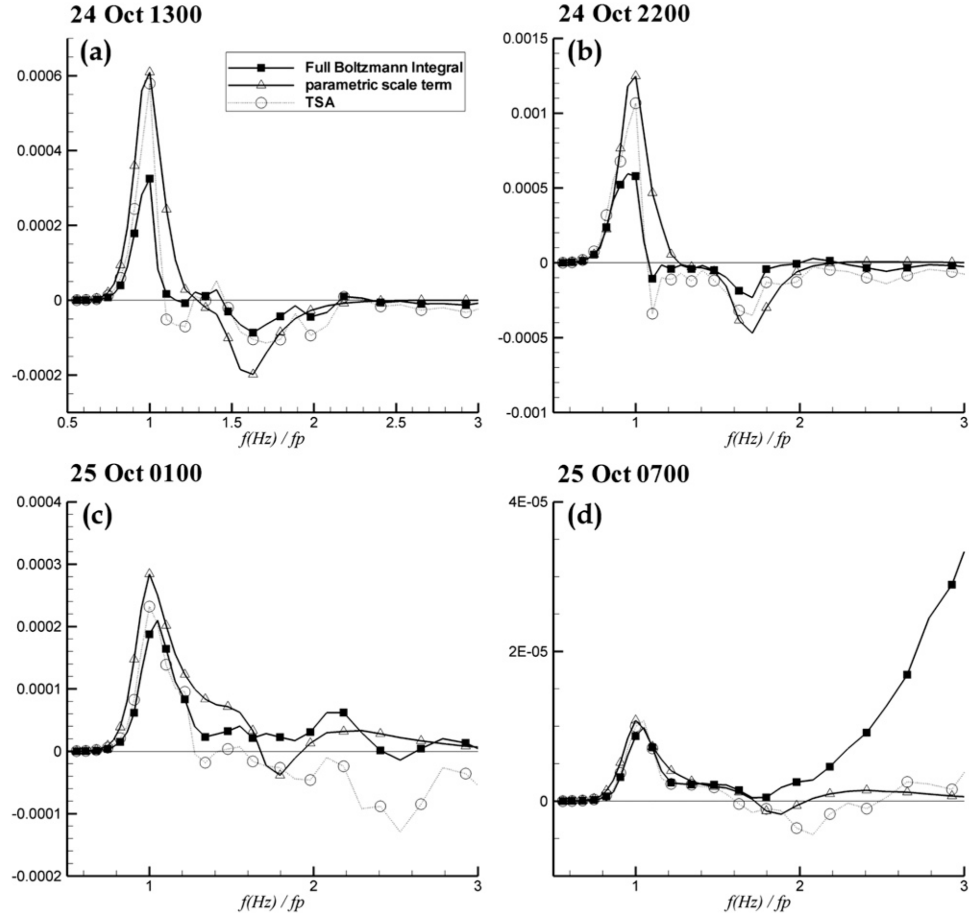

FIG. 12. The 1D energy transfers (m^2 Hz^{-1} s^{-1}) from TSA and FBI for the four cases shown in Figs. 9 and 10.

the order of one-half of those for the DIA. These results show no apparent variation with time.

Relative to the FBI, Fig. 15c shows that the TSA has correlation coefficients near unity for the entire spectrum as a function of time, for most of the test period, from 0700 EST 24 October until 0700 EST 25 October. This ''overall'' correlation coefficient decreases toward the end of the time series to about 0.5, reflecting a similar decrease in correlation coefficients for the TSA for the equilibrium regions of the spectra (as indicated in Fig. 15). Corresponding correlation coefficients for the forward-face and rear-face regions of the spectra for the TSA are almost unity for all of the simulation.

By comparison, correlation coefficients for the DIA are lower, achieving about 0.2–0.3 overall for the entire spectrum, for the entire time series. Correlation coefficients for the DIA have different values for different regions of the spectrum. For the forward-face region, the correlation coefficients of the DIA to the FBI vary from about 0.3 to 0.7; for the rear-face region, they vary from about −0.2 to 0.5. For the equilibrium-range region, they vary from about −0.7 to +0.3.

5. A mixed sea and swell episode

The version of the TSA presented here is based on a unimodal spectral decomposition. Thus, a potentially challenging test might be a situation in which the sea and swell peaks are not too far removed from each other. Such a case occurred shortly after Wilma passed by the Outer Banks of North Carolina, when the directional spectra evolved briefly into a classic situation with mixed sea and swell. Figure 16 shows a sequence of three directional spectra for 1300–1446 EST 25 October. As can be seen, the energy spectra become bimodal with two almost equal peaks at 1353 EST. The low-frequency swell component is approaching the coast from 165° at a peak frequency of about 0.068 Hz while the local seas are coming from a more northerly direction (135°) with a peak frequency of about 0.9 Hz.

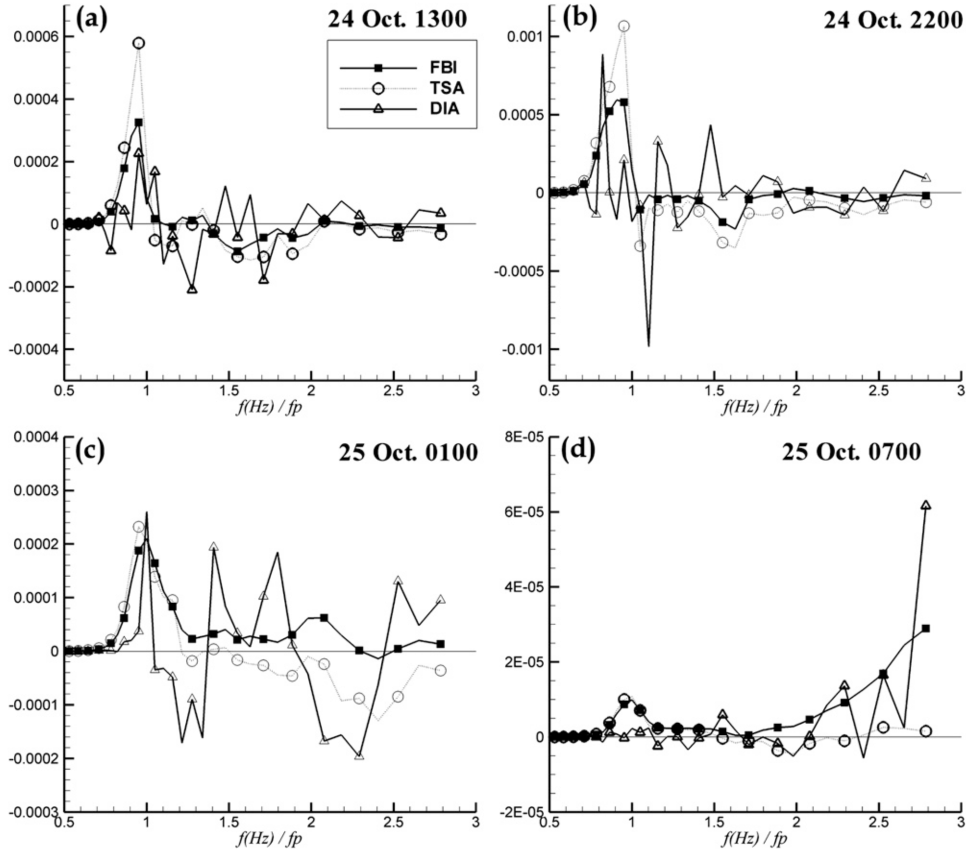

FIG. 13. The 1D energy transfers ($m^2\ Hz^{-1}\ s^{-1}$), comparing TSA, FBI, and DIA, for the four cases shown in Figs. 9 and 10.

Figure 17 shows the decomposition of the directionally integrated spectra in normalized (or compensated) form in the three panels on the left; the frequency regions lower than the wind-sea spectral peak ($f/f_p < 1$) are expanded in the three panels on the right in Fig. 17. As can be seen, even though the swell peak at 1353 EST (middle panel in Fig. 17) is as large as the sea peak, the sea peak is much larger in terms of its compensated values. Therefore, the nonlinear interactions are expected to be much larger in the vicinity of the sea peak than in the vicinity of the swell peak. Figure 18 shows the comparison of the TSA and the FBI results for this set of spectra, confirming that the interaction rates are very small in the vicinity of the swell peak. It also can be seen in Fig. 18 that the local-scale term in the TSA nudges the results into closer correspondence to the FBI. Moreover, as can be seen in Fig. 19, the TSA performs much better than the DIA in the low-frequency portion of the spectrum. This result is obtained despite the use of a single-peaked parametric form in the spectral decomposition for the TSA formulation. Frequency regions below the wind-sea spectral peak ($f/f_p < 1$) are expanded in the three panels on the right in Figs. 18 and 19.

6. Discussion

We have presented evidence that the TSA appears to work relatively well even for observed spectra that deviate strongly from the ''best fit'' two-variable parameterization of the directional spectrum. Two aspects of our comparisons provide interesting insights into the overall role of nonlinear interactions in evolving wave fields. First, we have observed that the effect of angular energy distributions (which vary as a function of frequency) is much more substantial than might be expected from past studies. For example, much of the mathematical basis for the role of wave–wave interactions in developing distinct equilibrium characteristics within a spectrum, such as the equilibrium-range f^{-4} form, was built using the assumption of isotropic energy distributions with angle (Webb 1978; Zakharov and Filonenko 1966; Resio and Perrie 1989). Scaling concepts for directionally integrated transfers of energy based on these theories have been assumed to be only minimally affected by variations in the angular distribution when generalizing the application of these scaling laws to anisotropic cases. While this approach may be appropriate for classes of angular spectral energy distributions that are constant with frequency (i.e., $\cos^{2n}\theta$), our results clearly show that angular distributions of energy that vary with frequency can affect the directionally integrated transfers by more than a factor of 2. Even in apparently symmetric situations, such as the development of waves along a very long fetch with winds blowing normal to the coast, the fact that the directional distribution develops pronounced bimodal lobes at high frequencies (Long and Resio 2007) changes the transfer rates significantly in the spectral peak region. Moreover, this type of variation in scaling cannot be reproduced by approximations that use constant geometric sampling in their formulation; in the latter approach only a subset of all possible four-wave interactions is used to estimate the nonlinear wave–wave interactions term S_{nl}, such as most versions of the DIA currently used in operational modeling.

Second, results in section 5 show that nonlinear interactions predicted by the DIA deviate significantly from the FBI solutions for swell portions of wave spectra (Fig. 13d). Although these nonlinear interactions are typically very small, as estimated by the DIA within existing third-generation models, the evolution of swell on oceanic scales can be significantly affected by these interactions. Let us consider an idealized case of a very large storm that is assumed (to a first approximation) to be homogeneous in the direction orthogonal to the main wind direction, with very small gradients in the along-wind direction, over distance Δx. The time over which the effects of dispersion remains relatively small and can be estimated by

$$t \approx \frac{\Delta x}{c_g(f_1) - c_g(f_2)},$$

where f_1 and f_2 are the upper and lower frequency bounds on the main energy-containing region of the spectrum, respectively. If we take this region to be bounded by the domain from $0.8f_p$ to $1.5f_p$ and Δx to be 1500 km, the effects of dispersion will be relatively small for about 60 h of propagation time. Although we expect gradients in energies within the wave fields to be important in most situations, this simplified situation allows us to examine the role of nonlinear transfers on the evolution of the spectrum.

Assuming an f^{-4} initial spectrum following Eq. (17) in Part I, we started with an initial wave height of 13.7 m and a peak period of 14.3 s. Although the wave–wave interactions are themselves conservative in these simulations, they produce a persistent cascade of energy into very high frequencies. Since the energy levels in the high-frequency range are capped by an f^{-5} tail set to a fixed level in our FBI formulation, similar to conventional wave models, energy that is fluxed into this region of the spectrum is assumed to be lost as a result of wave breaking and other dissipative processes. We find that in our FBI simulations the spectral peak downshifts to peak periods of 16.4 s within 3 h of elapsed time, 17.5 s within 8 h of elapsed time, and 18.7 s after 23 h of elapsed time. Simultaneously, the wave height diminished from its initial value to 13.0 m after 3 h, 12.6 m after 8 h, and 12.1 m after 23 h. Obviously, this type of evolution is important to swell arrival times, peak periods, and wave heights.

It is clear from the previous discussion that nonlinear interactions in swell can play an important role in swell evolution at oceanic scales. It is also clear that the nonlinear interactions diminish substantially with time and occur on a much slower time scale than the interactions that affect local seas in a wave-generation area. Therefore, and as a consequence of the results in section 5, interactions between swells and local seas tend to be much smaller than interactions among the spectral components of the local sea itself. Given these two points, it appears that future operational versions of the TSA should utilize existing algorithms for separating wave spectra into sea and swell components. Such a separation process should use a decomposition that allows for consideration of multiple peaks while neglecting interactions among the isolated portions of the spectrum.

7. Conclusions

In this paper we have presented comparisons between three formulations—the TSA, DIA, and FBI—using observed wave spectra from Currituck Sound described by Long and Resio (2007) and directional waverider data from open-ocean conditions at a location off the U.S. Army Field Research Facility at Duck collected during Hurricane Wilma in 2005. The Currituck Sound data involve deep-water fetch-limited conditions, in onshore- and offshore-propagating wave conditions and slanting-fetch conditions, with significant wave heights up to 0.5 m. Open-ocean directional wave spectra collected during Hurricane Wilma are waverider observations. The latter data included maximum wave heights of about 4.2 m during continuously changing winds involving wind-generated growing waves, and sea–swell interactions.

The TSA formulation involves functional decompositions of given wave spectra. It is important for the parametric terms in the spectral decomposition to capture much of the broad-scale behavior of the spectra. However, as has been shown here, even for relatively

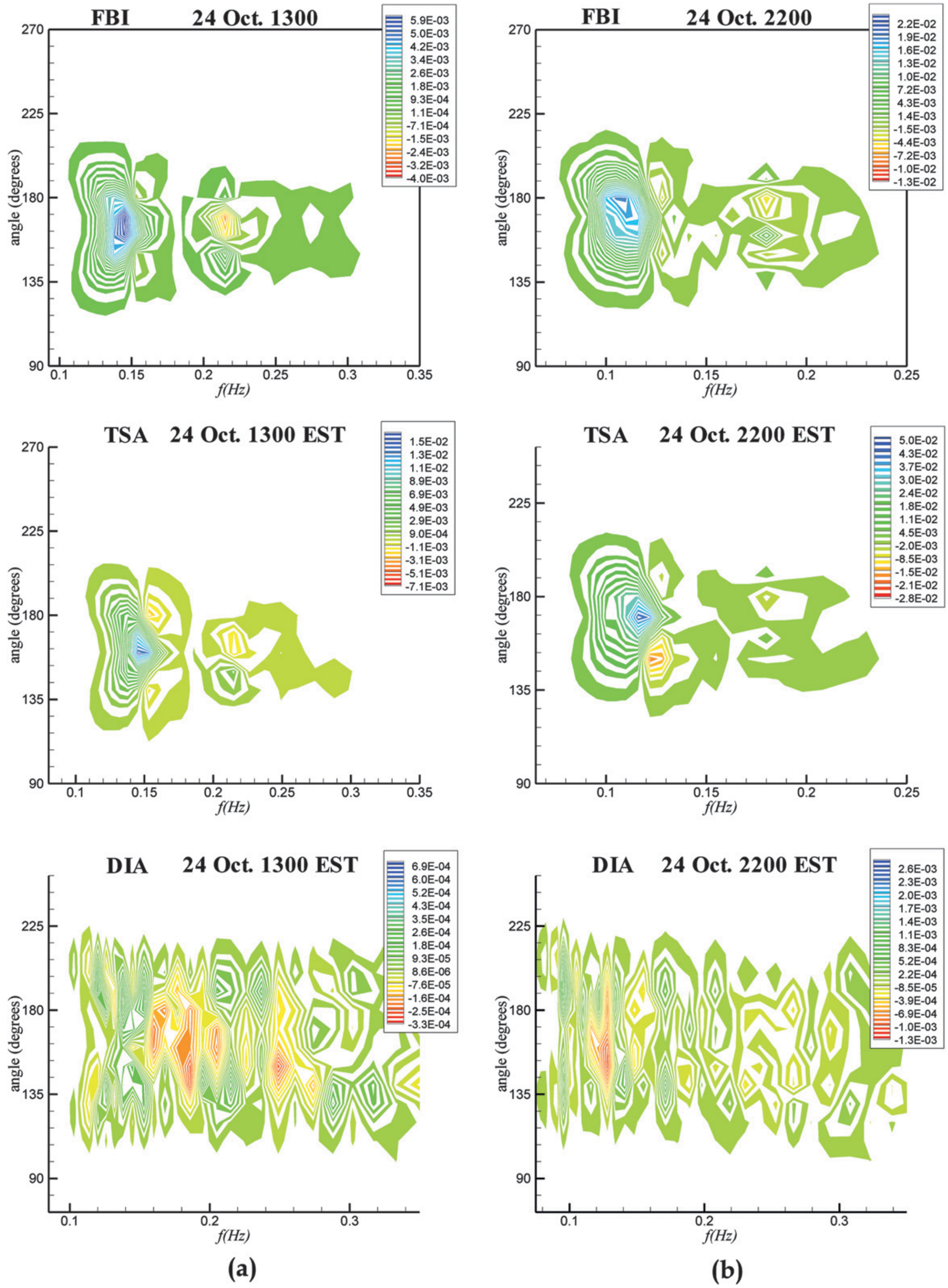

FIG. 14. Results in 2D ($m^2\ Hz^{-1}\ s^{-1}\ {}^{\circ -1}$) comparing (top) FBI, (middle) TSA, and (bottom) DIA from spectra shown in Fig. 9–10 for (a) 1300 EST 24 Oct, (b) 2200 EST 24 Oct, (c) 0100 EST 25 Oct, and (d) 0700 EST 25 Oct.

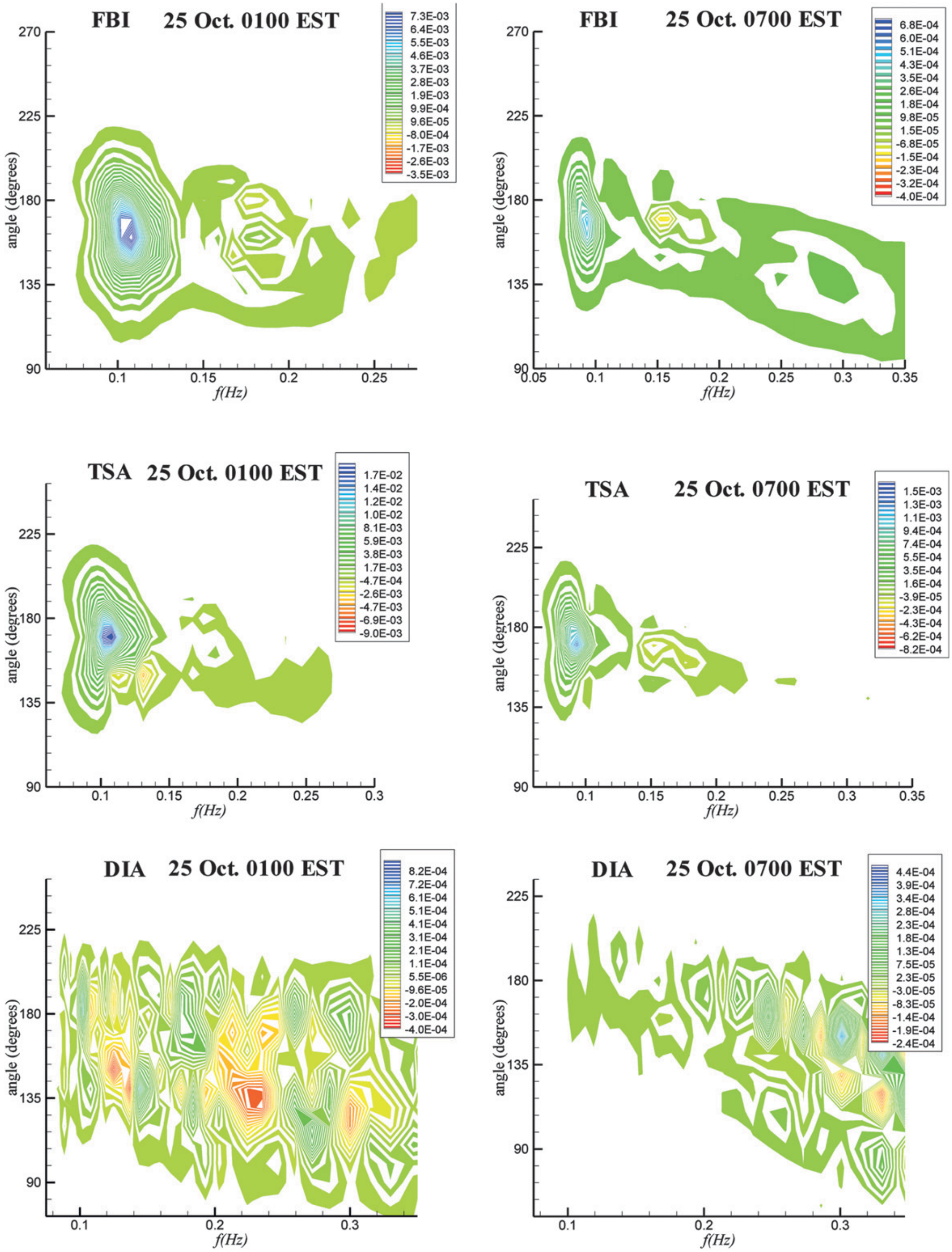

(c) (d)

FIG. 14. (*Continued*)

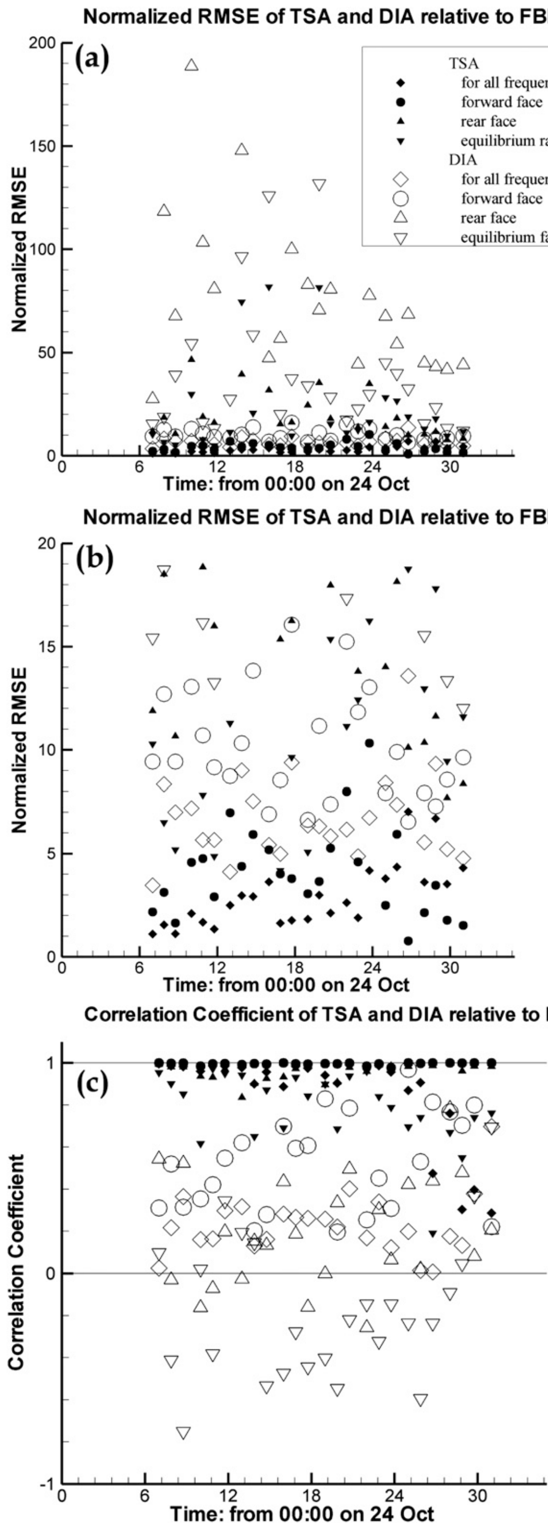

FIG. 15. (a) Error calculations showing NRMSE of TSA and DIA relative to FBI for the Hurricane Wilma waverider spectra cases; (b) blown-up image of lowest part of (a). (c) Error calculations for nonlinear transfer for all Hurricane Wilma spectra in (a) and (b) showing correlation coefficients.

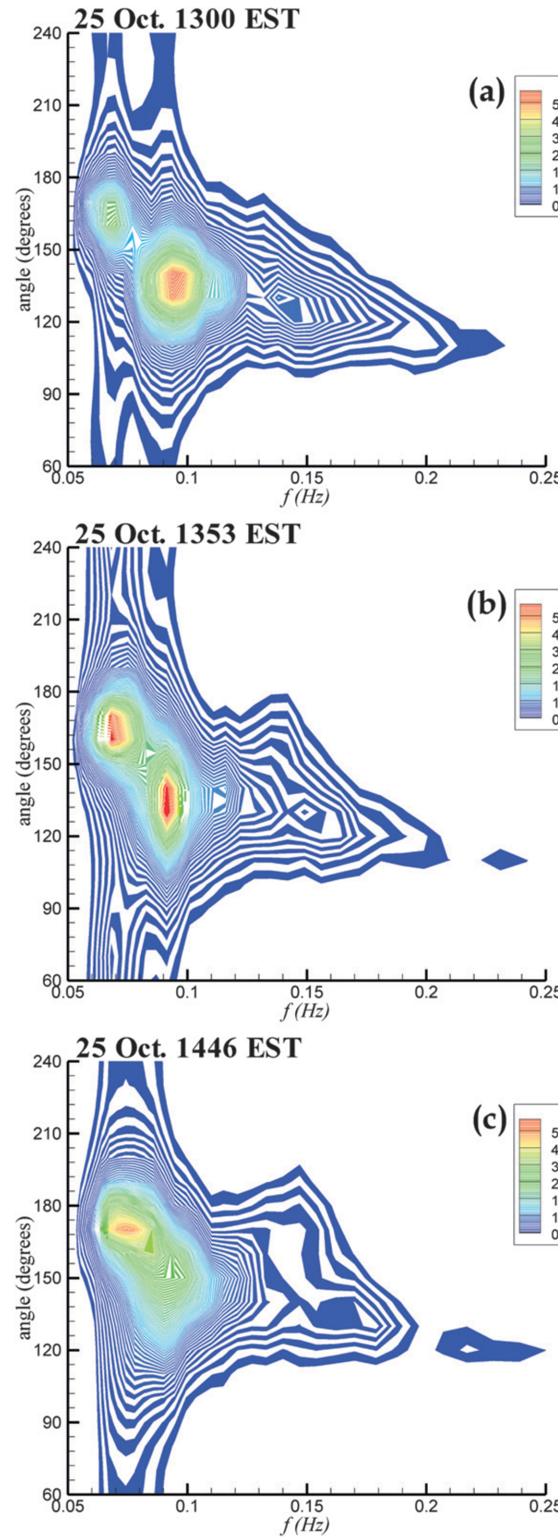

FIG. 16. Two-dimensional wave energy spectra $E(f,\ \theta)$ ($m^2\ Hz^{-1}\ s^{-1}\ {}^{\circ -1}$) observed by the directional waverider moored off Duck during Hurricane Wilma (time and date indicated in each panel) for (a) developing swell spectra, (b) wind-sea and swell interactions, and (c) completion of swell–wind-sea interactions.

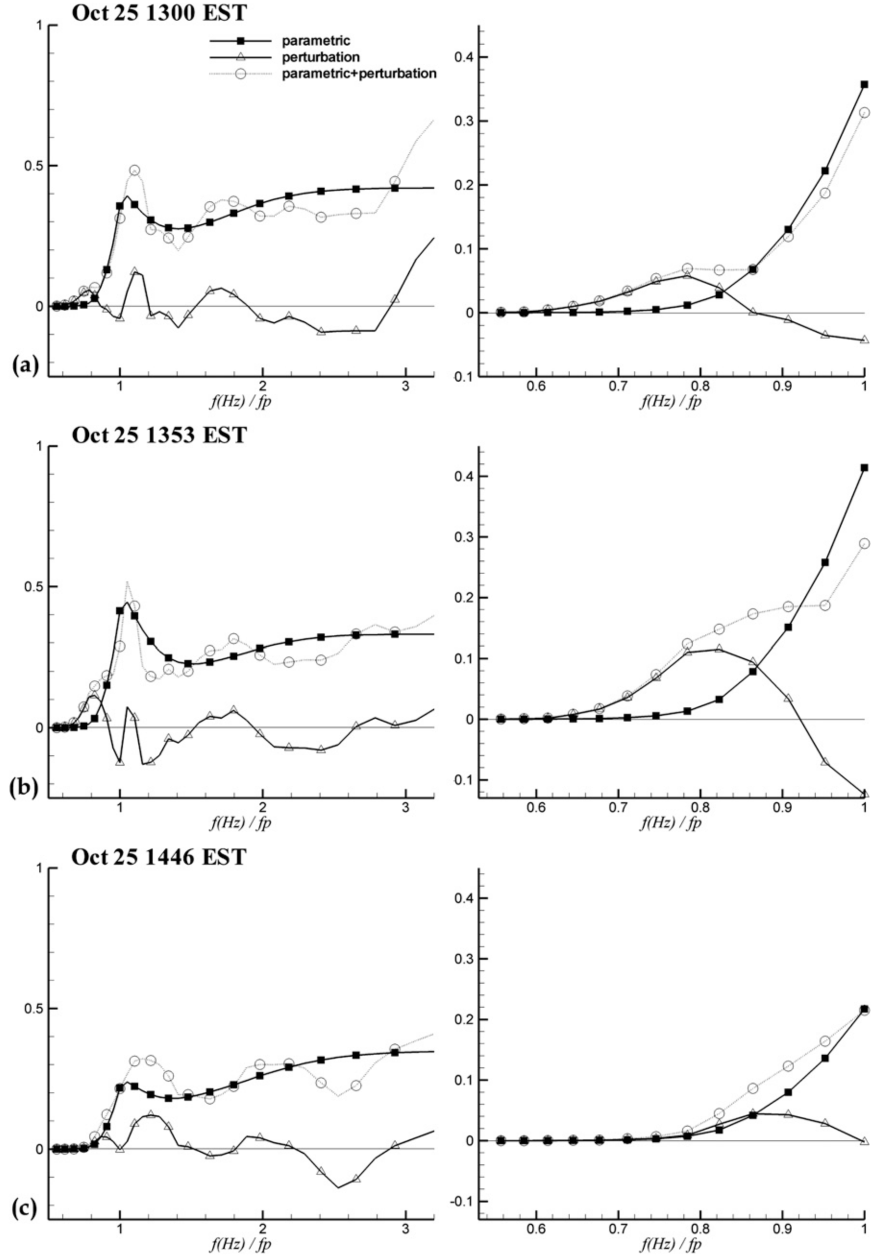

FIG. 17. The 1D energy decompositions for construction of TSA for the three waverider cases in Fig. 16, for wind-sea and swell interactions, showing the parametric term, perturbation function, and 1D energy spectrum (parametric + perturbation). These terms are normalized by ω^4 as representative of the equilibrium-range variation. Panels on the right side are blown-up images of the low-frequency portions of the corresponding panels on the left side.

complicated cases in which observed spectra deviate significantly from simple parametric forms (either in their directional distributions of energy or their directionally integrated shapes), the perturbation component of the TSA appears to do a relatively good job of forcing the total TSA solution toward the FBI solution. Thus, the latter is critical to the representation of nonlinear transfers in observed spectra, since it is highly unlikely that the parametric form can capture all of the important directional features of the spectral shape, which can affect nonlinear transfer rates and in turn influence wave evolution.

In each class of both the Currituck wave spectra and the waverider spectra from Hurricane Wilma, the decomposition method resulted in relatively good TSA

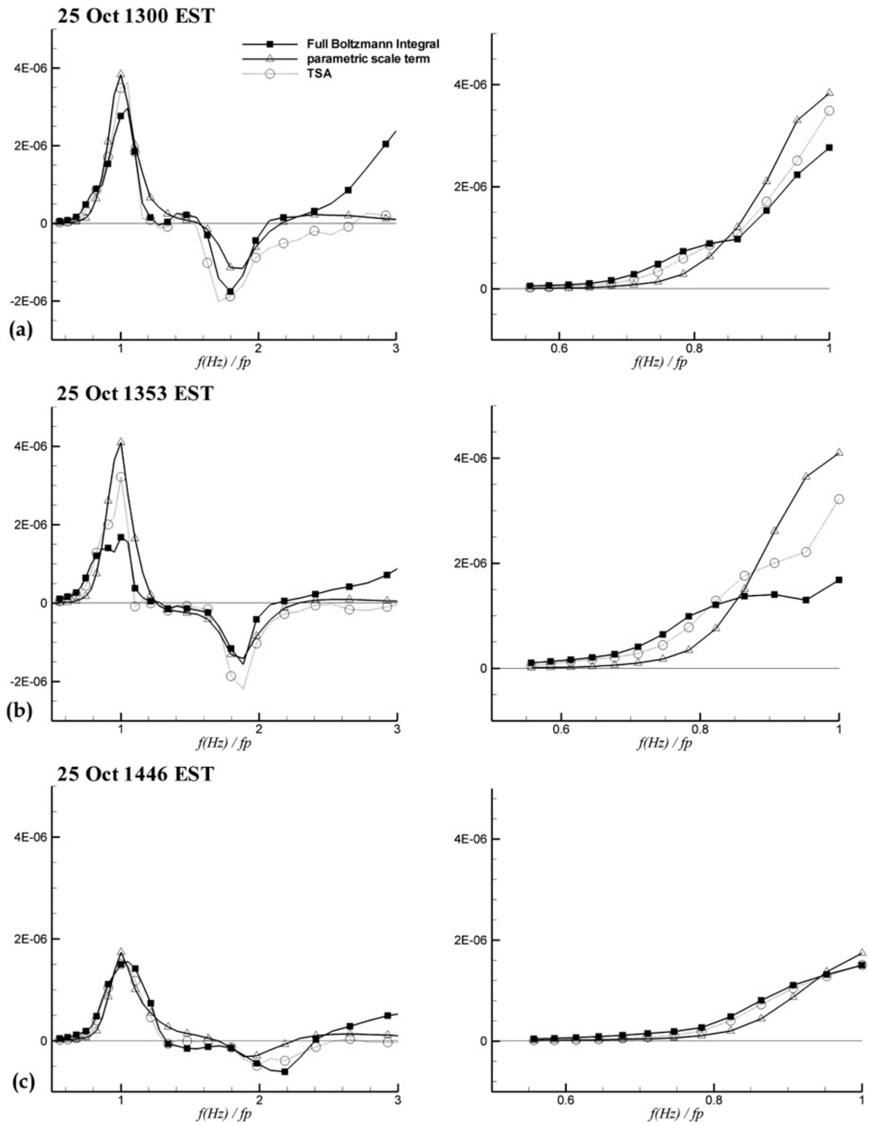

FIG. 18. The 1D energy transfer (m^2 Hz^{-1} s^{-1}) for TSA and FBI for the three spectral cases shown in Fig. 16. Panels on the right side are blown-up images of the low-frequency portions of the corresponding panels on the left side.

comparisons to the FBI results. In particular, the TSA was also applied to directionally sheared spectral examples from the Currituck dataset, in which the normalized spectral peak is largely absent because of the slanting-fetch–geometry, and Hurricane Wilma, in which waves were generated from continuously turning winds as the storm propagated past the buoy. In the latter case, the parametric function was shown to be able to represent the spectral peak and rear-face regions but not the entire equilibrium-range region. In this case, a departure of the parametric function from the highly sheared portion of the spectrum occurred at the very highest frequencies. In comparisons from Currituck wave classes or Hurricane Wilma data, the 1D and 2D results from the TSA and FBI compare relatively well, particularly in the forward-face region of the spectrum. Overall, the two formulations also exhibited similar features for the other regions of the spectrum—for the rear face and the equilibrium range—and in the directional distributions associated with these regions.

However, while the DIA achieves some approximate comparison with the FBI in 1D comparisons for the forward face, rear face, and equilibrium range, it is not competitive with the TSA and correlates poorly with the FBI. In the 2D results, the DIA suggests positive and negative regions of transfer rates with incorrect

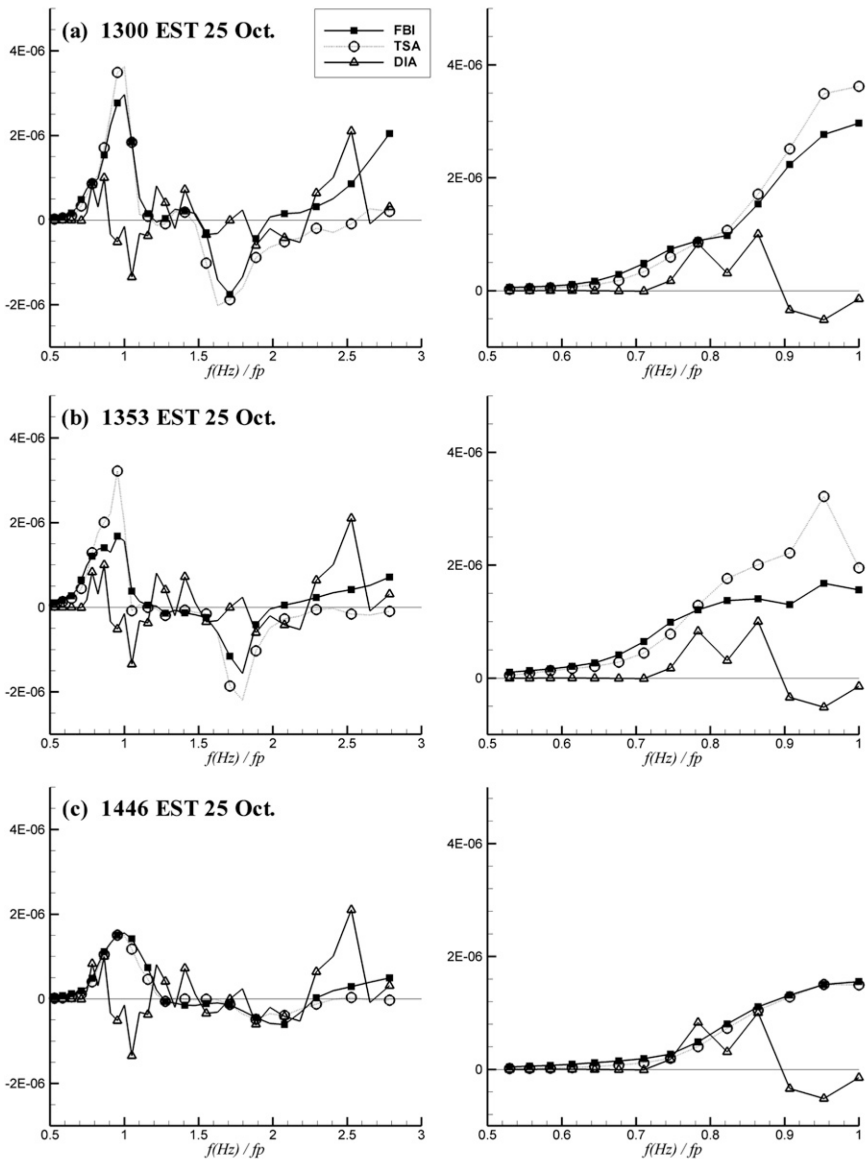

FIG. 19. Comparisons of 1D transfer ($m^2\ Hz^{-1}\ s^{-1}$) from FBI, TSA, and DIA, for the three cases shown in Fig. 16 from Hurricane Wilma. Panels on the right side are blown-up images of the low-frequency portions of the corresponding panels on the left side.

magnitudes and locations, in comparison with the FBI. Specifically, the DIA exhibits less prominence of regions of positive transfer rates, in comparison with the TSA or FBI results. The qualitative features for the DIA are sufficiently dissimilar relative to the FBI that differences are very large. In highly sheared spectra, the TSA achieves a relatively good comparison to the FBI, although there is increasing divergence in the two formulations for higher frequencies in the equilibrium range. However, the DIA fails to capture the main FBI variations for the forward-face or rear-face regions and diverges significantly from the FBI in the equilibrium range.

Statistical results show that the TSA compares favorably to the FBI and that it is a notable improvement over results attained by the DIA. For Currituck Sound data, NRMSEs for the TSA relative to the FBI are about one-half of those resulting for the DIA. Associated correlation coefficients for the TSA are near unity, whereas correlation coefficients for the DIA are about 0.5. For Hurricane Wilma wave data, NRMSE values for the TSA are also about one-half of those resulting for the DIA. Correlation coefficients for the TSA are almost unity, computed for the entire spectrum, for almost the entire test period from 0700 EST 24 October until

0700 EST 25 October, decreasing toward the end of the test period to about 0.5. This trend reflects the tendency for TSA correlation coefficients for the equilibrium region to slightly decrease toward the end of the test period. By comparison, overall correlation coefficients for the DIA are lower, achieving about 0.2–0.3 for the entire spectrum, for the entire time series.

The current version of the TSA has a unimodal basis in the broad (first) spectral scale of the approximation. Thus, one question that might be posed concerns the applicability of this version of the TSA to multimodal distributions of spectral energy. How well does the TSA work for situations with multiple peaks within the distribution of energy in the spectrum (i.e., classical mixed sea and swell situations)? Our results show that the TSA does surprisingly well for these spectral examples. This is the case, in part, because the second (local) scale of the approximation appears to capture some of the contributions of the swell to the total interactions. In part, it is also due to the fact that the interactions in the swell portion of the spectrum, and also the influence of the interactions between swell and sea spectral frequencies, are much smaller than the interactions within the sea spectral region.

Our results also shed some light on the fundamental scaling of nonlinear interactions and the role of nonlinear interactions in the evolution of swell over long distances. Presently, most theoretical work on the characteristic equilibrium ranges and energy fluxes is based on assumed isotropic angular distributions of energy in a spectrum. These results have been extended to anisotropic spectra by assuming that the directional distributions do not markedly affect the scaling laws. Here, we have shown that this assumption does not appear to be generally valid for frequency-dependent angular distributions of energy. Furthermore, we show here that nonlinear interactions, although relatively small in the low-frequency swell portion of the spectrum, likely play an important role in the evolution of swell on a global scale. Since the DIA does not correctly represent these interactions, its application to long-distance swell propagation appears to have serious limitations. Clearly these issues are ongoing concerns for future work. How can TSA be applied to simulations of evolving spectra with interacting sea and swell? Future studies will involve simulations of developing sea states, using simple idealized academic cases as pioneered in the Sea Wave Modelling Project (SWAMP; SWAMP Group 1985), as well as more challenging real-ocean conditions. The latter will involve simple wave development cases driven by relatively constant wind fields, as well as more complicated sea and swell interaction cases involving marine storms such as Hurricane Wilma. These studies will try to show that the TSA is capable of replicating spectral development as observed by field measurements, in comparison with accepted baseline operational wave models.

Acknowledgments. Support for this research comes from the U.S. Army Corps of Engineers MORPHOS program, Canadian Panel on Energy Research and Development (PERD—Offshore Environmental Factors Program), and the National Oceanographic and Atmospheric Administration via the Southeast University Research Association Coastal Ocean Observing and Prediction (SCOOP) program. The authors also acknowledge the Office, Chief of Engineers, U.S. Army Corps of Engineers, for permission to publish this paper.

REFERENCES

Donelan, M. A., J. Hamilton, and W. H. Hui, 1985: Directional spectra of wind-generated waves. *Philos. Trans. Roy. Soc. London,* **A315,** 509–562.

Ewans, K. C., 1998: Observations of the directional spectrum of fetch-limited waves. *J. Phys. Oceanogr.,* **28,** 495–512.

Hasselmann, K., and Coauthors, 1973: Measurements of wind-wave growth and swell decay during the Joint North Sea Wave Project (JONSWAP). *Deutsch. Hydrogr. Z.,* **A8** (Suppl.), 1–95.

Hasselmann, S., and Coauthors, 1988: The WAM model—A third-generation oceans wave prediction model. *J. Phys. Oceanogr.,* **18,** 1775–1810.

Long, C. E., 1995: Directional wind wave characteristics at harvest platform. U.S. Army Corps of Engineers Tech. Rep. CERC-95-4, 182 pp.

——, and D. T. Resio, 2007: Wind wave spectral observations in Currituck Sound, North Carolina. *J. Geophys. Res.,* **112,** C05001, doi:10.1029/2006JC003835.

Longuet-Higgins, M. S., D. E. Cartwright, and N. D. Smith, 1963: Observations of the directional spectrum of sea waves using the motions of a floating buoy. *Ocean Wave Spectra,* Prentice-Hall, 111–136.

Pawka, S. S., 1983: Island shadows in wave directional spectra. *J. Geophys. Res.,* **88,** 2579–2591.

Resio, D. T., and W. Perrie, 1989: Implications of an f^{-4} equilibrium range for wind-generated waves. *J. Phys. Oceanogr.,* **19,** 193–204.

——, and ——, 2008: A two-scale approximation for efficient representation of nonlinear energy transfers in a wind wave spectrum. Part I: Theoretical development. *J. Phys. Oceanogr.,* **38,** 2801–2816.

Resio, R. T., C. E. Long, and C. L. Vincent, 2004: Equilibrium-range constant in wind-generated wave spectra. *J. Geophys. Res.,* **109,** C01018, doi:10.1029/2003JC001788.

SWAMP Group, 1985: *Ocean Wave Modelling*. Plenum Press, 256 pp.

Wang, D. W., and P. A. Hwang, 2001: Evolution of the bimodal directional distribution of ocean waves. *J. Phys. Oceanogr.,* **31,** 1200–1221.

Webb, D. J., 1978: Non-linear transfers between sea waves. *Deep-Sea Res.,* **25,** 279–298.

Young, I. R., L. A. Verhagen, and M. L. Banner, 1995: A note on the bimodal directional spreading of fetch-limited wind waves. *J. Geophys. Res.,* **100,** 773–778.

Zakharov, V. E., and N. N. Filonenko, 1966: The energy spectrum for stochastic oscillation of a fluid's surface. *Dokl. Akad. Nauk SSSR,* **170,** 1992–1995.